2012

Agglomeration, Evaporation And Morphological Changes In Droplets With Nanosilica And Nanoalumina Suspensions In An Acoustic Field

Erick Tijerino
University of Central Florida

AGGLOMERATION, EVAPORATION AND MORPHOLOGICAL CHANGES IN DROPLETS WITH NANOSILICA AND NANOALUMINA SUSPENSIONS IN AN ACOUSTIC FIELD

by

ERICK GIOVANNI TIJERINO CAMPOLLO
B.S. Universidad del Valle de Guatemala, 2008

A thesis submitted in partial fulfillment of the requirements
for the degree of Master of Science in Aerospace Engineering
in the Department of Mechanical, Materials and Aerospace Engineering
in the College of Engineering and Computer Science
at the University of Central Florida
Orlando, Florida

Fall Term
2012

Major Professor: Dr. Ranganathan Kumar

ABSTRACT

Acoustic levitation permits the study of droplet dynamics without the effects of surface interactions present in other techniques such as pendant droplet methods. Despite the complexities of the interactions of the acoustic field with the suspended droplet, acoustic levitation provides distinct advantages of controlling morphology of droplets with nanosuspensions post precipitation. Droplet morphology is controlled by vaporization, deformation and agglomeration of nanoparticles, and therefore their respective timescales are important to control the final shape. The balance of forces acting on the droplet, such as the acoustic pressure and surface tension, determine the geometry of the levitated droplet. Thus, the morphology of the resultant structure can be controlled by manipulating the amplitude of the levitator and the fluid properties of the precursor nanosuspensions. The interface area in colloidal nanosuspensions is very large even at low particle concentrations. The effects of the presence of this interface have large influence in the properties of the solution even at low concentrations.

This thesis focuses on the dynamics of particle agglomeration in acoustically levitated evaporating nanofluid droplets leading to shell structure formation. These experiments were performed by suspending 500μm droplets in a pressure node of a standing acoustic wave in a levitator and heating them using a carbon dioxide laser. These radiatively heated functional droplets exhibit three distinct stages, namely, pure evaporation, agglomeration and structure formation. The temporal history of the droplet surface temperature shows two inflection points. Morphology and final precipitation structures of levitated droplets are due to competing mechanisms of particle agglomeration, evaporation and shape deformation. This thesis provides

a detailed analysis for each process and proposes two important timescales for evaporation and agglomeration that determine the final diameter of the structure formed. It is seen that both agglomeration and evaporation timescales are similar functions of acoustic amplitude (sound pressure level), droplet size, viscosity and density. However it is shown that while the agglomeration timescale decreases with initial particle concentration, the evaporation timescale shows the opposite trend. The final normalized diameter hence can be shown to be dependent solely on the ratio of agglomeration to evaporation timescales for all concentrations and acoustic amplitudes. The experiments were conducted with 10nm silica, 20nm silica, 20nm alumina and 50nm alumina solutions. The structures exhibit various aspect ratios (bowls, rings, spheroids) which depend on the ratio of the deformation timescale (t_{def}) and the agglomeration timescale (t_g). For $t_{def}<t_g$ a sharp peak in aspect ratio is seen at low concentrations of nanosilica which separates high aspect ratio structures like rings from the low aspect ratio structures like bowls and spheroids. The time duration of pure evaporation, agglomeration and structure formation are presented in phase diagrams where these stages are represented by regions in the time-particle concentration domain. A comparison of phase diagrams for different particle solutions is made illustrating the influence of liquid properties on the duration of the structure formation phases and the transition to different morphology when concentration is increased.

A mi abuelita Dorita,

lamento no haber terminado a tiempo…

ACKNOWLEDGMENTS

I would like to express my most sincere gratitude to my advisor, Dr. Ranganathan Kumar, for the opportunity to work in his state of the art laboratory, for his financial support, for making me part of his prestigious research group and for pushing me past what I thought I was capable off. I also like to show my appreciation to my co-advisor, Dr. Sarpashi Basu, for his mentoring and his invaluable contributions which have undoubtedly improved the quality of this research work. I want to thank the members of our research group, Dr. Abhishek Saha for his collaboration and for all the constructive discussions we had over the course of this work, James Wilson for his contribution measuring solution properties which were key to perform the analysis presented in this thesis, Dr. Eshan Yakhshi-Tafti, Dr. Gu Xin, Ben Patrick and Joshua Lee for your friendship and support. It is true that we stand in the shoulders of giants and what we achieve as a group is greater than what we can accomplish individually, that makes me very proud to be part of this exceptional group of people. I am also grateful for the financial support of the department of Mechanical and Aerospace Engineering at the University of Central Florida that supported me and my research during part of my graduate studies.

During the course of my academic and professional career I have been lucky to have friends that have been my mentors, I want to show my appreciation to Pablo Rousselin and Luis Zea for inspiring me, for showing me the way by example and for making me stride to be a better person. And of course none of this would haven possible without the love and unconditional support of my parents, I want to thank them for always being there for me and for encouraging me to achieve what I put my mind into.

TABLE OF CONTENTS

LIST OF FIGURES

LIST OF SYMBOLS & ABBREVIATIONS

u_{max}	Acoustic field maximum velocity.
SPL	Acoustic field Sound Pressure Level.
Ω	Acoustic field wave number.
Ma	Acoustic Mach number.
t_g	Agglomeration time scale.
P_B	Bernoulli under-pressure.
CO_2	Carbon dioxide.
t_{def}	Deformation time scale.
L_r	Transducer to reflector distance.
C	Droplet aspect ratio.
a	Droplet major axis half length.
b	Droplet minor axis half length.
t_e	Evaporation time scale.
P_o	Far field gas phase pressure.
fps	Frames per second.
μ_o	Gas phase dynamic viscosity.
υ_o	Gas phase kinematic viscosity.
γ_o	Gas phase specific heat ratio.
G	Gibbs free energy.
IR	Infrared.

$\dot{\gamma}$	Internal recirculation flow shear rate.
$\acute{\psi}$	Internal recirculation stream function.
u_l	Internal recirculation velocity scale.
D/D_o	Non-dimensional droplet diameter.
PIV	Particle Image Velocimetry.
r_p	Particle radius.
φ	Particle volume concentration.
P_R	Radiative pressure.
t_g/t_e	Ratio of agglomeration to evaporation time scales.
κ	Ratio of gas to liquid phase viscosity.
SEM	Scanning electron microscopy.
μ_o	Solution dynamic viscosity.
c_o	Speed of sound.
∂	Stokes boundary layer thickness.
t_f	Structure formation time.
σ	Surface tension.
S	System entropy.

CHAPTER I: INTRODUCTION

Acoustic levitation permits the study of droplet dynamics without the effects of surface interactions present in other techniques such as pendant droplet methods. Despite the complexities of the interactions of the acoustic field with the suspended droplet, acoustic levitation [1-4] provides distinct advantages of controlling morphology of droplets with nanosuspensions post precipitation [5-9]. Droplet morphology is controlled by vaporization, deformation and agglomeration of nanoparticles, and therefore their respective timescales are important to control the final shape. The balance of forces acting on the droplet, such as the acoustic pressure and surface tension, determine the geometry of the levitated droplet. Thus, the morphology of the resultant structure can be controlled by manipulating the amplitude of the levitator and the fluid properties of the precursor nanosuspensions [10-15]. The interface area in colloidal nanosuspensions is very large even at low particle concentrations. The effects of the presence of this interface have large influence in the properties of the solution even at low concentrations. For example, the viscosity of a nanosilica solution at 2% concentration can be 40% higher than that of pure fluid [10-13].

Structure formation is a direct consequence of particle agglomeration, the rate at which particles agglomerate and the rate at which the liquid phase in the droplet evaporates determine the final structure size and morphology [16-17]. Agglomeration of suspended particles is an important field of study which delineates two processes called perikinetics and orthokinetics. The agglomeration of particles within an acoustically levitated droplet and its influence in structure formation has been studied previously by our group [18-19]. Perikinetics deals with

agglomeration of suspended particles due to Brownian rotation and diffusion, while orthokinetics arises from shear/velocity gradient within the liquid layers. Bremer et al [16] estimated the time scale of macroscopic aggregation which occurs when precipitation is visible. The number of bonds formed and aggregation rate are important for the aggregation process. This led them to define a physical time scale based on orthokinetic sedimentation which did not include arbitrary parameters like visibility of precipitation. The effect on structure geometry of agglomeration and evaporation rates is studied in this thesis by using the agglomeration and evaporation time scales. The objective is to acoustically levitate a droplet containing silica and alumina nanoparticle solutions at different concentrations heated by a CO_2 laser. This thesis analyzes the effect of concentration on the shape of final structure using high speed imaging and IR thermography. In a first attempt of this kind, the ratio of agglomeration to evaporation time, t_g/t_e, is used to compare the structure formation at different precursor concentrations, and is shown to influence the diameter ratio.

CHAPTER II: LITERATURE REVIEW

Nanofluids:

The term nanofluid refers to a colloidal suspension of nanometer size particles in a liquid phase. Nanofluids are comprised in the field of nanoscience which studies the phenomena that occurs at the one to one hundred nanometers [21]. The particles used in this study are of 10, 20 and 50nm size. To give a sense of scale, the diameter of a typical human hair is in the order of 80,000nm and most studied viruses are in the 20 to 100nm size scale. Stable colloidal suspension of nanoparticles is possible thanks to their small size and weight that allow fluid Brownian motion to significantly slow down particle deposition caused by gravitational force. The exceptionally large area to volume ratio of nanofluids means the interface area between nanoparticles and liquid in colloidal solutions is very large even at low particle concentrations. At a given total particle volume the total interface surface area increases exponentially with the decrease of particle size. A fixed volume of particles of nanometer scale have a surface area six orders of magnitude larger compared to the same volume of millimeter sized particles. In the particular case of a droplet containing a 5% volume concentration of 20nm particles, total surface area of the fluid, that comprises the droplet external and internal surface areas, is 1,300 times larger than the liquid surface area of the same size pure liquid droplet. Then interfacial phenomena at the liquid surface become a major factor that determines the state of the system due to the large magnitude of interfacial surface area in the system. Thus, surface dependent processes such as heat transfer are enhanced by the use of nanoparticles and the use of nanofluids as thermal fluids is a large application of nanotechnology. Also the energy at the interfaces

increases considerably since it is proportional to the interfacial area. The interface curvature at the particle surface is inversely proportional to the radius of the particle, as seen in figure 2.1. This makes the preparation of stable colloidal solutions with very small particles a challenge due to the very large surface free energy at the interface. The system will tend to equilibrium by minimizing its surface free energy and that causes particle agglomeration to reduce the interfacial surface area in order to minimize this interfacial energy. Then interfacial tension has to be reduced in order to have a stable suspension of very small particles, this is done by altering the surface properties of the particles, an example of this is the use of surfactants and dispersing agents. The many advantages that nanometer geometries bring come with the complexities of physical properties not being equal in the nano-scale compared to the macro-scale and give an opportunity to manipulate the properties of a fluid by their addition to the base fluid. The following sections present the effects of interfacial interactions on droplet geometry and its dependence on particle size and concentration.

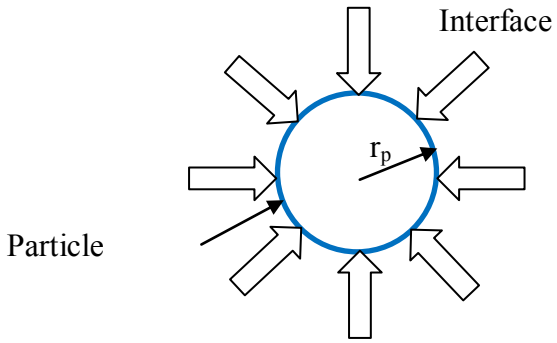

Figure 2.1: Nanoparticle Solid-Liquid Interface.

Acoustic Levitation:

Acoustic levitation permits the study of droplet dynamics without the effects of surface interactions present in other techniques such as pendant droplet methods. These advantages do not come without compromise; acoustic levitation brings complexities due to the interactions of the acoustic field with the suspended droplet. Internal flow and droplet rotation is induced by acoustic streaming; also droplet deformation is caused due to the effect of acoustic pressure at the droplet surface. Acoustic levitation is a powerful tool to investigate droplet phenomena, but the effects of this method has on the subject of study must be determined and quantified in order to correlate the results to applications outside of an acoustic field.

Acoustic levitation is accomplished by generating a standing acoustic wave; this is done by the emission of pressure pulses from a transducer that are reflected by a static surface placed at a distance L_r from the transducer. The incident and reflected pressure waves superimpose to form a harmonic standing acoustic wave. The acoustic field force potential makes sample suspension possible, this potential is the combination of radiation pressure "P_R" and Bernoulli pressure "P_B" of the standing wave [9]. The gradients of the force potential are the source of the axial and radial levitation forces acting on the droplet. In the absence of gravity, droplets can be suspended in the pressure nodes of the standing wave. In the gravitational field, the droplet center of gravity moves below the pressure node to compensate for the droplet weight, as seen in figure 2.2.

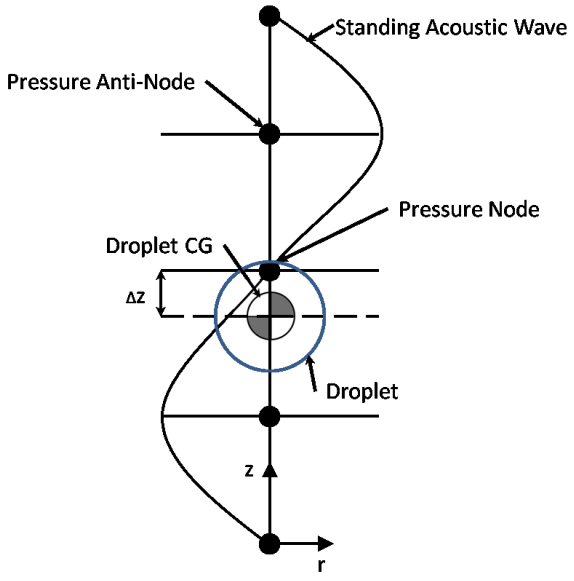

Figure 2.2: Sketch of Droplet Positioning in the Standing Acoustic Wave

In order to suspend a droplet, the acoustic wave pressure amplitude has to balance the droplet weight. If the amplitude is lower than this critical value, levitation is not possible. The levitation force acting on the droplet also depends on its external area, which in turn depends on droplet volume, thus the limits for levitation are determined by the density of the droplet. Droplets suspended in an acoustic field are subject to deformation from the pressure forces acting at the surface applied by the acoustic field. The geometry of the suspended droplet depends on the equilibrium of forces normal to the surface and forces acting on the surface tangential direction, the later will be addressed in more detail in the following sections. The amplitude of the acoustic field correlates with sound pressure level (SPL) measured in decibels (dB). Radiation and Bernoulli pressure can be calculating by the following [9]:

$$P_R = -P_B = 0.5 P_o \gamma_o M a^2 \tag{2.1}$$

Where Ma is the acoustic Mach number and correlates to SPL approximately by:

$$\mathrm{SPL} \approx 197 + 20 \log \mathrm{Ma} \tag{2.2}$$

The acoustic pressure acting on the droplet tends to flatten it deforming it from a spherical to an oblate geometry. In the case where the acoustic forces acting in the normal direction of the droplet surface exceed the forces acting tangential to the surface, i.e., if a droplet has very low surface tension or if the droplet is in an acoustic field at high SPL, droplet disintegration may occur. The acoustic pressure limit after a droplet goes through break up is dictated by the size and interfacial properties of the droplet. Anilkumar, Lee and Wang [22] have studied the conditions at which acoustically levitated droplets become unstable and break up, they have studied the balance of stresses applied on the levitated droplets and have determined that the geometry and stability of acoustically levitated droplets depend on surface tension, acoustic pressure and droplet size with respect to the acoustic wave number. They have observed droplet deformations including horizontal elongation, appearance of concavities in the upper and lower halves of the droplet and "dog-bone" cross section droplets. Then by varying the acoustic levitation conditions, the geometry of the suspended droplets can be manipulated and droplet disintegration can be avoided or promoted depending on the requirements of the particular application. The important effect of droplet geometry in the final geometry of agglomerated nanoparticles is presented in the following sections.

Acoustic Streaming

When an object is suspended in an acoustic field the presence of this object perturbs the force potential field around it. This perturbation results in a flow around the suspended object, which is termed 'Acoustic Streaming'. This phenomenon has been studied by many authors. In particular, Lord Rayleigh was the first one to publish his calculations of fluid motion via the momentum equation of steady incompressible laminar flow in 1884 [23]. Burdukov and Nakoryakov (1965) [24] and Lee & Wang (1990) [25] applied perturbation methods to solve the acoustic streaming flow field, Riley (1997) [26] differentiated the internal acoustic streaming due to interactions with a solid surface from the acoustic streaming caused by dissipation to the bulk. Acoustic streaming is the fluid motion that occurs due to the attenuation of high intensity ultrasound waves [27]. This attenuation can be caused by dissipation in the far field, referred as "quartz wind", it can also occur due to the presence of a solid boundary. In this study, it is assumed the acoustic waves do not penetrate the liquid droplet due to the much larger sonic impedance of the fluid phase compare to the gas phase sonic impedance. Thus a suspended liquid droplet is considered to be a solid boundary within the acoustic field [5, 7]; the ultrasonic waves are then dissipated at the Stokes boundary layer around the "solid" surface of the droplet. The acoustic energy is dissipated in the form of heat and by transferring momentum to the fluid in the dissipation region [5, 7, 28, 29]. This transference of momentum puts the fluid surrounding the surface of droplet in motion. Yarin et.al. [5, 7] addressed the streaming phenomena around an acoustically levitated droplet and obtained solutions of the boundary layer equations around the droplet. Two regions were identified: the inner acoustic streaming referred as acoustic boundary layer due to solid wall dissipation at the surface of the droplet, which its thickness is in the order

of $\delta = (2\nu_o/\omega)^{1/2}$, and outer acoustic streaming due to far field dissipation where vortices are of the order of several droplet diameters [7]. The later type of recirculation is of great importance in the case of evaporating droplets since the vapor coming from the droplet can be transported by the outer streaming away from the droplet which has an effect on the evaporation rate due to the vapor concentration reduction near the droplet surface. The acoustic streaming field is illustrated in figure 2.3.

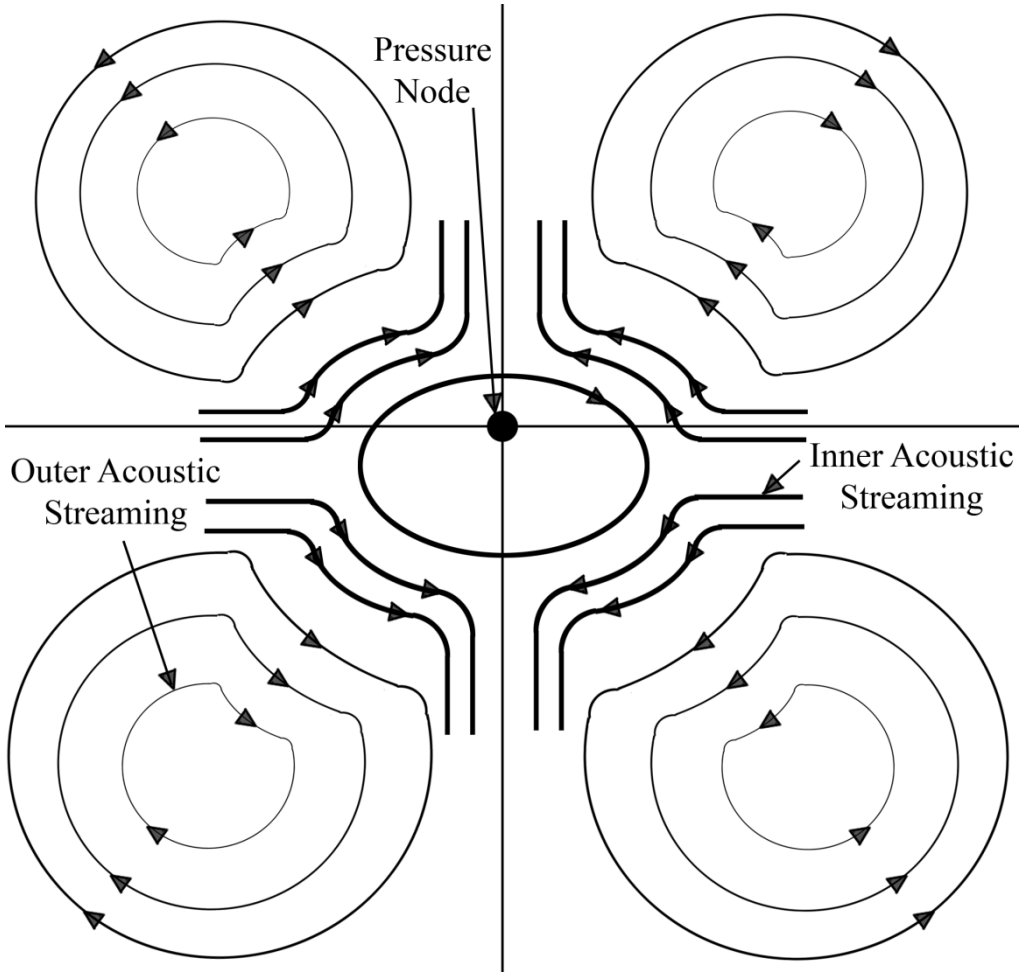

Figure 2.3 Sketch of Acoustic Streaming Flow Field [7].

A secondary flow around the droplet is also present and it is referred as secondary acoustic streaming. This flow at the droplet surface, acts tangentially on the droplet in the horizontal direction rotating the suspended droplet. In the experimental and numerical work of a droplet resting on a flat surface is subject to an acoustic field, Algane et.al.'s [29] results illustrate the secondary acoustic streaming around the droplet. The flow at the surface of the droplet causes recirculating internal flow in the droplet. In the work done by Hong Zao et.al. [30], the circulation within the droplet is described by the steady state streaming function in polar coordinates of the flow in the droplet, $\acute{\psi}$.

$$\acute{\psi} = \frac{9|M|\kappa}{\sqrt{2}(80+32\kappa)}(r^3 - r^5)\bar{\mu}(1 - \bar{\mu}^2) \tag{2.3}$$

where M is a constant parameter determined by the acoustic wave frequency and the droplet radius, $\bar{\mu}$ is the cos(θ) and κ is to the ratio of gaseous and liquid media dynamic viscosity.

$$\kappa = \mu_o/\mu_l \tag{2.4}$$

where μ_o is the dynamic viscosity of the gaseous media and μ_l is the dynamic viscosity of the liquid media inside the droplet. This ratio decreases with increasing liquid viscosity, by assuming the viscosity of the fluid in the droplet does is not a spatial dependant and assuming constant gaseous phase viscosity it can be said the recirculation velocity field scales to:

$$u_l \sim \sqrt{\frac{1}{\mu_l}} \sim \sqrt{\kappa} \tag{2.5}$$

Then the recirculation velocity scale "u_l" decreases with liquid phase viscosity, this has a significant effect on the distribution of a solute inside the droplet. Figure 2.4 a. and b. illustrate

the internal flow induced through shear by primary and secondary acoustic streaming. The solution of the stream function shows two recirculating cells at the top and two cells at the bottom of the droplet. In a microgravity environment, where the droplet is located at the pressure node, these cells are symmetrical. The gravitational forces acting on the droplet in terrestrial conditions shift the droplet under the pressure node making the bottom recirculation cells larger than the top cells [8]. Figure 2.4.a is an illustration of the symmetrical recirculation cells reported in Rednikov et al. analytical study of a non-rotating droplet [8]. Secondary acoustic streaming over imposes a horizontal circulating flow, shown in figure 2.4.b. Droplet solid rotation is can be caused by droplet misalignment with the levitation axis, solution inhomogeneity and/or asymmetric heating [18]. In the work of Saha et al., the flow regime inside the droplet has been measured via Particle Image Velocimetry (PIV), the results of those measurements show that droplet rotation affects internal recirculation causing only one recirculation cell to be present in the droplet [18, 21]. The important effects of these internal flows on particle migration in the droplet are discussed in later sections.

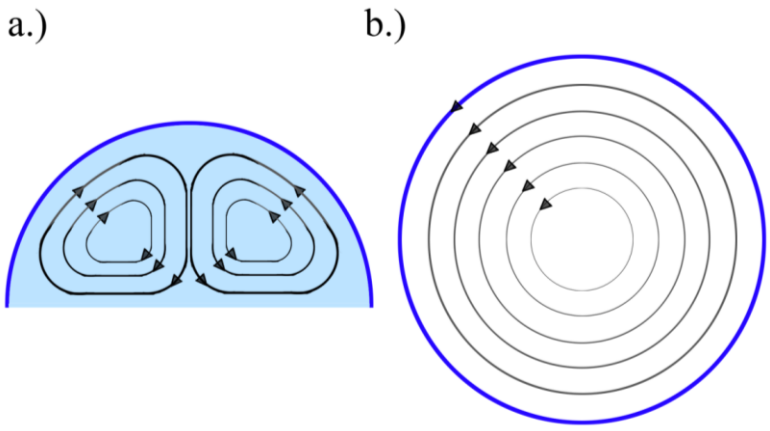

Figure 2.4: a) Droplet Cross Section View Illustrating Internal Recirculation Cells due to primary Acoustic Streaming. b) Droplet Top View Illustrating Horizontal Rotating Flow Induced by Secondary Acoustic Streaming.

Interface Physical Properties

Surface tension is defined by the free energy at the interface of the fluid due to the lack of other molecules at one side of the interfacial boundary. The energy at the interface is referred as Gibbs free energy. The solutions used in the present work are water based thus the intermolecular attraction properties of this substance are discussed in this section. Water has a relatively high surface tension (~72mN/m) compared to any organic compound. These particularly high attraction forces are due to water's molecular structure, water molecules form hydrogen bonds with four other surrounding water molecules. The energy of these bonds (10-40kJ/mol) is larger than the usual Van der Waals attraction energy (~1kJ/mol) but much lower than ionic bonds (~500kJ/mol) [31]. Surface tension is thermodynamically defined as Gibbs free energy by interface unit area. Gibbs free energy can be defined as the amount of energy to create a unit of surface area; it can be expressed at constant pressure and temperature as [21]:

$$\sigma = \frac{\partial G}{\partial A}\Big|_{T,P} \tag{2.6}$$

Where σ is surface tension, G is Gibbs free energy and A is surface area. In the particular case of enlarging the surface of a sphere the work done on the droplet to change its radius by ∂r can be written as [29]:

$$F\partial r = \sigma \partial A \tag{2.7}$$

Then the energy needed to deform a spherical droplet, which has the lowest surface area for any given volume, can be quantified by equation 2.7. Surface tension is proportional to Gibbs

free energy at the interface, the thermodynamic definition of Gibbs free energy can be expressed as [32]:

$$G = U - TS + PV \tag{2.8}$$

If we take the derivative of Gibbs free energy:

$$\partial G = \partial U - TdS - S\,\partial T + P\,\partial V + V\,\partial P \tag{2.9}$$

Since $\partial U = T\,\partial S - P\,\partial V$ we substitute in (2. 8):

$$\partial G = V\,\partial P - S\,\partial T \tag{2.10}$$

At constant pressure (2.9) yields:

$$\left.\frac{\partial G}{\partial T}\right|_P = -S \tag{2.11}$$

To satisfy equilibrium conditions the entropy of the system has to be at a maximum and Gibbs free energy at a minimum. At equilibrium, entropy is constant so a change in Gibbs free energy scales with temperature (at constant pressure) as:

$$\Delta G \sim -\Delta T \tag{2.12}$$

Since surface tension is proportional to the variation of Gibbs free energy $\sigma \sim G$, an increase in temperature causes a decrease in surface tension thus a decrease in surface energy at the interface. Then it can be said, from a thermodynamic point of view, that surface tension is free energy per unit of interfacial surface area. These interfacial effects also take place in solid-

liquid interfaces; surface tension in this case is referred as interfacial tension which is a more general way to refer to this phenomenon.

Effects of Interface Curvature

The curvature of an interface has significant effects on some of the thermal properties of the fluid and on the surface forces acting at the interface [29, 33]. This is particularly true for small geometries since their surface to volume ratio and the curvature of their interfaces can be very large. A pressure difference between the exterior and the interior of the droplet occurs when the interface is curved. In order for the system to be in equilibrium the forces acting tangentially to the surface have to be balanced by the difference in pressure across the interface. The pressure difference across the interface Δp can be calculated equating the force exerted on a surface element of the surface $\Delta p \partial A$ to the force acting on a line at the surface by surface tension, $\sigma \partial l$, the result is the Laplace equation:

$$\Delta \mathrm{p} = \sigma \left(\frac{1}{\mathrm{r}_1} + \frac{1}{\mathrm{r}_2} \right) \tag{2.13}$$

Where r_1 and r_2 are the radii of curvature of the surface, in the case of a spherical geometry r_1 and r_2 are equal. Then the pressure difference at the interface is not only a function of interfacial energy but is also a function of the curvature of the interface. Curvature also has an effect on thermodynamic properties of the interface, from equation 2.9 it can be seen that Gibbs free energy has a PV component, then for a constant temperature and surface area a change in Gibbs free energy can be expressed as:

$$\Delta G = V \Delta P \tag{2.14}$$

Substituting 2.13 for a spherical droplet of radius r in 2.14 yields:

$$\Delta G = V\sigma\left(\frac{1}{\mathrm{r}}\right) \tag{2.15}$$

Then Gibbs free energy increases with curvature of the interface (1/r), this increase of free energy is known as the Gibbs-Thompson effect [29, 33, 34]. Taking into consideration the physico-chemical and mechanical equilibrium conditions, the following expression for vapor pressure can be derived from the Laplace equation [29, 33]:

$$ln\left(\frac{p^c}{p^\infty}\right) = \left(\frac{\sigma V}{RT}\right)\left(\frac{2}{r}\right) \tag{2.16}$$

Where p^c is the vapor at a curved surface and p^∞ is the vapor pressure of the same substance in a flat surface of zero curvature. This expression is known as Kelvin's equation and it represents the dependence of vapor pressure on the curvature of the interface surface. Then from this relation it can be said that vapor pressure increases with surface curvature thus vapor pressure is higher for smaller droplets. This explains why in a distribution of different size droplets the large droplets will increase in size by absorbing the smaller droplets [29, 33].

Equilibrium of Multiphase Multicomponent Systems

Multi-component systems including more than one phase are stable when all the component phases are in equilibrium. The phases in the system can be considered as subsystems, all subsystems have to be in equilibrium with each other for the whole system to be in equilibrium. The free energy of the each subsystem can be quantified applying the definition of Gibbs free energy:

$$dG^{\alpha} = -S^{\alpha}dT + V^{\alpha} + \mu_1^{\alpha}dn_1^{\alpha} + \mu_2^{\alpha}dn_2^{\alpha} \quad (2.17)$$

$$dG^{\beta} = -S^{\beta}dT + V^{\beta} + \mu_1^{\beta}dn_1^{\beta} + \mu_2^{\beta}dn_2^{\beta} \quad (2.18)$$

Where α and β represent the phases in the system, 1 and 2 refer to the components in the system, μ is the chemical potential of each component at a given phase and n is the number of moles of a component at a given phase. If there is no source nor a sink in the system, the amount of matter lost by a phase, due to a phase change, is gained by the phase it changes into

$$dn_i^{\beta} = -dn_i^{\alpha} \quad (2.19)$$

The total change of free energy of the system is the sum of free energy change of each subsystem. For the system to be in equilibrium free energy has to be at a minimum, $dG = 0$. The free energy change of the system can be then expressed as:

$$dG = dG^{\alpha} + dG^{\beta} = 0 \quad (2.20)$$

At constant temperature and pressure and if component 2 is kept at a constant physical state, $dn_2^{\alpha} = dn_2^{\beta} = 0$, substituting 2.17, 2.18 and 2.19 into 1.20 after rearranging yields:

$$\mu_1^{\alpha} = \mu_1^{\beta} \quad (2.21)$$

This states the chemical potential of each component is equal in all phases in order for the system to be in equilibrium. If this condition is not satisfied, mass will change from one phase to the other [29]. To calculate the composition of a two-phase system, an approximation using known properties of the pure components can be used when the system is at relativity low pressure. From equation 2.21 we can write for component 1:

$$\bar{f}_1^{\alpha} = \bar{f}_1^{\beta} \tag{2.22}$$

Where $\bar{f}$ is the fugacity of component 1 in the mixture, taking the particular case of a liquid-vapor system, then

$$\bar{f}_1^{L} = \bar{f}_1^{V} \tag{2.23}$$

The fugacity of a component can be quantified as product of the molar fraction of the component in the system by the fugacity of the component in pure form *f*.

$$\bar{f}_1^{L} = \chi_1 f_1^{L} \tag{2.24}$$

The fugacity of the component can be approximated as to be equal to the component saturation pressure $f_1^{L} = p_1^{sat}$, if we approximate the fugacity of the component to be equal to the saturation pressure of the component in the system $\bar{f}_1^{L} = \bar{p}_1^{sat}$, we can write

$$\bar{p}_1^{sat} = \chi_1 p_1^{sat} \tag{2.25}$$

This relation is known as Rault's Law, where $\bar{p}_1^{sat}$ is the vapor pressure of the component, the vapor pressure of the system is the sum of the vapor pressure of each component in the system. In the particular case where one of the components is non-volatile, its vapor pressure is zero and the system vapor pressure will be equal to the product of the saturation pressure of the volatile component by its molar fraction. Since $\chi_1 + \chi_2 = 1$ and increase of molar concentration of component 2 will decrease component's 1 molar fraction thus decreasing the vapor pressure of the system.

CHAPTER III: METHODOLOGY

The experimental set up consisted of an ultrasonic levitator (Tec5 ultrasonic levitator, 100 kHz) to suspend the droplet (Figure 3.1) [15]. The suspended droplet was heated by a CO_2 laser irradiating at a wave length of 10.6 μm with a nominal beam diameter of 2 mm. The power of the laser was tuned at 0.75 MW/m^2 using a power supply controller. An Infrared camera was placed perpendicular to the laser beam to measure the temperature of the droplet. The IR camera (FLIR Silver: calibrated for a range of -5 to 200^oC with an accuracy of +/- 1^oC) was equipped with a microscopic zoom (FLIR G3-F/2) lens to facilitate 3X magnification with a working distance of 40 mm. The IR camera was operated at a 100 fps and the recorded images were processed to obtain the temperature data of the droplet during heating. The integration time of the IR camera depends on the temperature range adapted. Most of the experiments were performed with a temperature range of 20-80^oC which needed an integration time of 1.63 msec. The error in temperature detection due to change in emissivity was found to be 0.03 °C and hence negligible. A high speed camera (Fastec TSHRMM, with a maximum speed of 16000 frames per second) along with a zoom lens assembly (Navitar 6000) was used to capture the physical processes within the droplet during the laser irradiation. This camera was placed at an angle of 30^0 with the laser beam as shown in Figure 3.1. The event was recorded at 500 fps, the maximum that could be achieved without losing spatial resolution. The images from high speed camera were used to measure the instantaneous diameter of the droplet with a better time resolution than the IR camera (100 fps).

Particles of different types and size were used in this work, 10nm and 20nm Silica as well as 20nm and 50nm Alumina. Experiments were conducted at particles concentrations of ϕ = 0.5, 1, 2, 3 and 5%vol in addition to these the maximum concentrations attainable from the colloidal suspensions manufacturer were used. In the case of 10nm Silica the maximum concentration used was φ = 7.33%vol, 20nm Silica φ = 23.11%vol, 20nm Alumina φ = 8.99%vol and 50nm Alumina φ = 5.99%vol. The experiments were conducted with four different types of particles, six particle concentrations and three SPL (160, 162 and 165dB) for each particle type. In addition, glycerin was added to 0.5 and 2%vol 10nm Silica (1 and 4%vol glycerin concentrations respectively) solutions to study the effect of increasing the solution viscosity on structure formation. Similarly surfactant was added to 10nm and 20nm Silica particle concentration φ = 0.5%vol solutions to observe the effect of surface tension reduction on the final structure morphology. The droplets were generated and deployed to the pressure node of the levitator by a micro needle. For every run of the experiment, the initial diameter of the droplet was maintained to be 500 μm (+/- 30 μm). After the experiment, the IR and high speed images were analyzed to obtain the temperature and diameter data.

The temperature data was obtained by defining a zone of interest around the surface of the droplet in each IR images, and the maximum, average and standard deviation of the temperature within droplet were calculated. It is important to mention here that the droplet oscillates from side to side with respect to the IR camera axis during the experiment resulting in out of focus images. For aforementioned analysis only those images were considered where the droplet was in the focus plane. The high speed images were used as evidence of different shape

transformations during the heating process. These images were also used to calculate the diameter of the droplet.

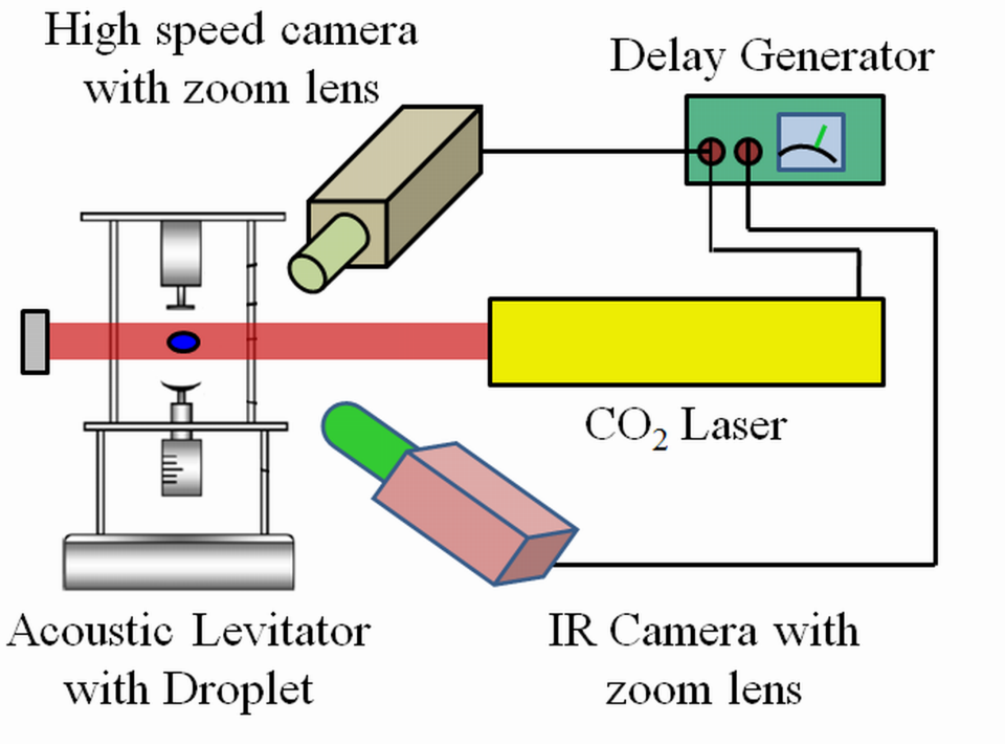

Figure 3.1: Experimental Setup Schematic.

The images were analyzed using Motion Measure software. To calculate the instantaneous diameter, an edge around the droplet was defined. An equivalent diameter was calculated from the area under the curve (edge) assuming the droplet to be axisymmetric with respect to the levitator longitudinal axis. The final form of the precipitate was collected on copper grids to perform ex-situ analyses. The samples were analyzed using optical microscope, and scanning electron microscopy (SEM). The schematic of the experimental setup is shown in Figure 3.1. More details about the experimental methods can be found in previous works [14,15].

CHAPTER IV: STRUCTURE FORMATION AT DIFFERENT ACOUSTIC AMPLITUDES

Radiatively heated levitated functional droplets exhibit three distinct stages namely pure evaporation, agglomeration and finally structure formation. During the initial stages of the vaporization process, the droplet surface temperature increases due to the monochromatic irradiation of the CO_2 laser. The increase in temperature is primarily due to the low vaporization rate and consequently transient heating of the droplet. The temperature front is initially asymmetric (due to directional laser flux) and subsequently advances over the surface (Figure 4.1). The droplet vaporization rate and temperature homogenization is mainly controlled by the forced convection caused by internal flow recirculation in the liquid phase induced by acoustic streaming (an effect caused by the scattering of the acoustic field due to the presence of the liquid droplet which has a large acoustic impedance compared to the gaseous phase, see Acoustic Streaming in Chapter 2) and droplet rotation about the vertical axis induced by the acoustic torque. Thus, acoustic levitation properties, such as sound pressure level (SPL), have a direct impact on liquid evaporation.

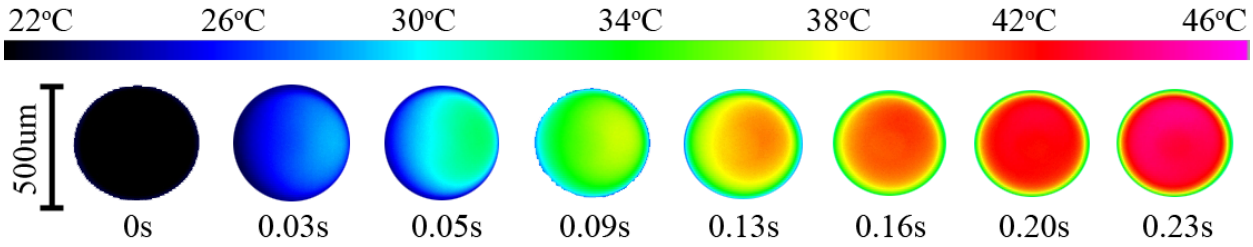

Figure 4.1: Infrared Images of the droplet temperature increase during early stages of the evaporation phase.

Characteristics of the temperature profiles

The droplet surface temperature profile exhibits a local maximum and a local minimum during the entire evaporation and agglomeration lifecycle (Figs. 4.2a and 4.3a). Initially with continuous heating, the temperature increases and reaches a maximum, which is a function of droplet specific heat, vapor pressure, latent heat, internal recirculation strength and projected area available for radiative heat transfer. Strong liquid phase recirculation induced by the acoustic streaming generally increases the timescale of the transient temperature rise or in other words, delays the occurrence of the first inflection point in the temperature profile (Figs. 4.2a and 4.3a). Internal recirculation also aids in reducing the diffusion length (increases the energy transport) and hence constrains the transient temperature rise of a droplet to a lower wet bulb limit. Thus, by tuning the sound pressure level, the magnitude of the acoustic streaming can be adjusted and hence one can control the wet bulb temperature and transient heating timescale. Hence the maximum temperature in the normalized time domain is higher at an SPL of 160 dB compared to 165 dB in the evaporation phase as shown in Figures 4.2a and 4.3a. Liquid evaporation is affected by SPL through heat transfer enhancement by virtue of strong recirculation. Once the droplet attains the wet bulb temperature, vaporization rate becomes maximum (first maximum of the temperature profile in Fig. 4.2a). However in radiatively heated droplets (unlike convectively heated droplets) the temperature increase leads to heat dissipation to the cooler ambient and heat transferred to the droplet is also converted to latent heat due to the phase change occurring at the droplet surface. The heat dissipated to the ambient combined with the latent heat of vaporization exceed the heat flow into the droplet from the heat source, then the net heat flow is in the direction away from the droplet causing a decrease in temperature.

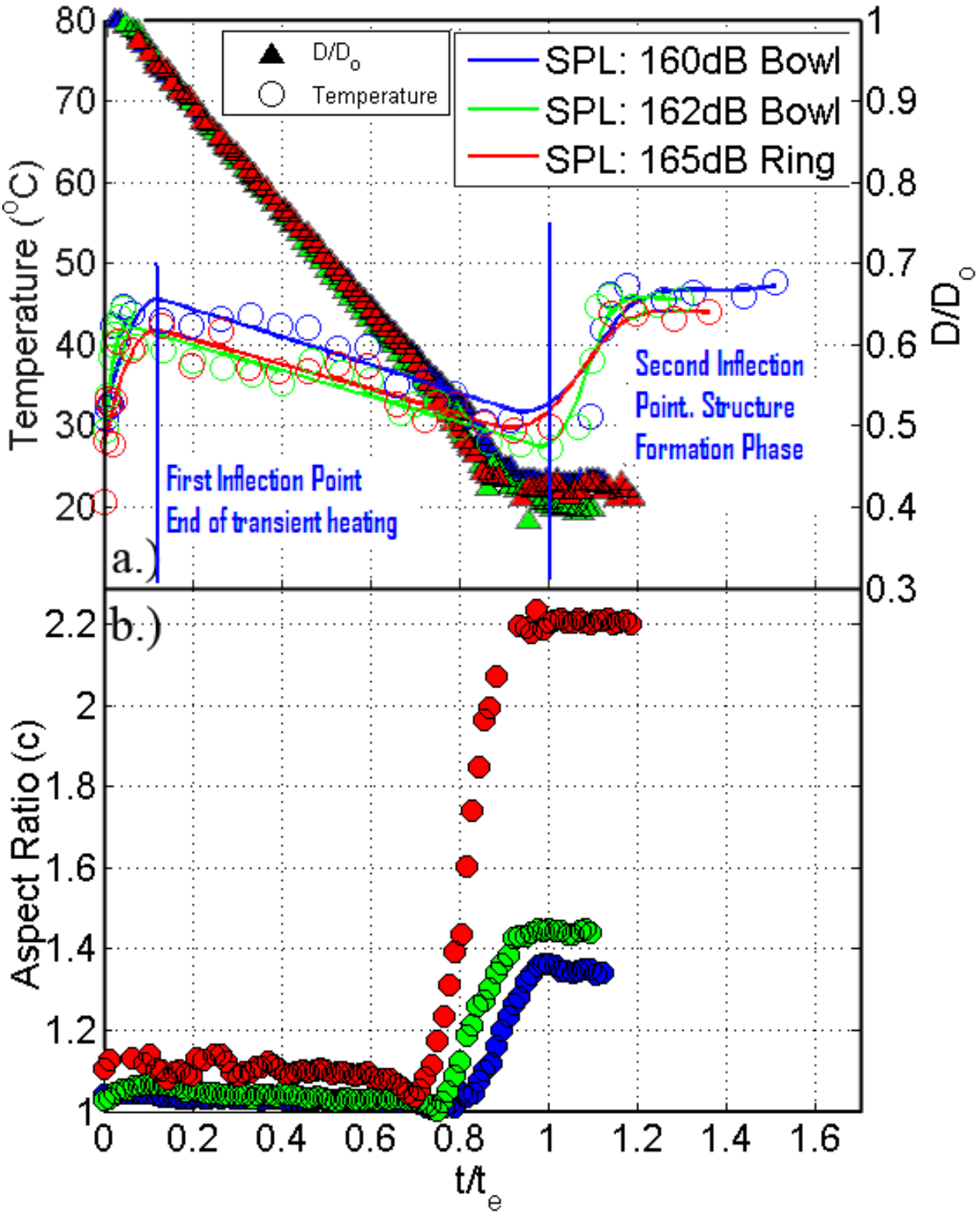

Figure 4.2: a) Surface Temperature and D/Do vs. t/t_e b) Aspect Ratio vs. t/t_e at $\varphi = 0.5\%$.

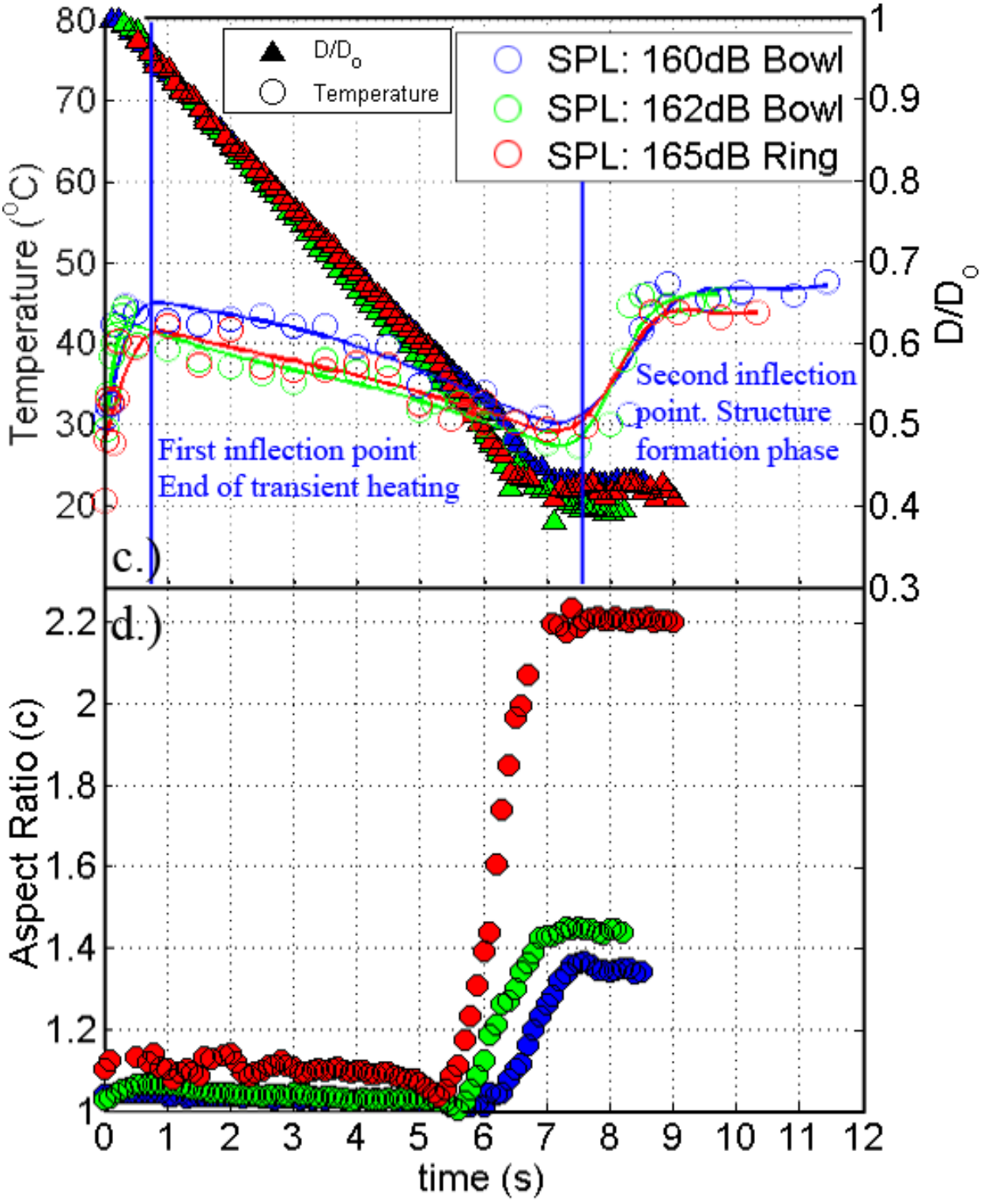

Figure 4.3: c) Surface Temperature and D/Do vs. time d) Aspect Ratio vs. time at φ = 0.5%.

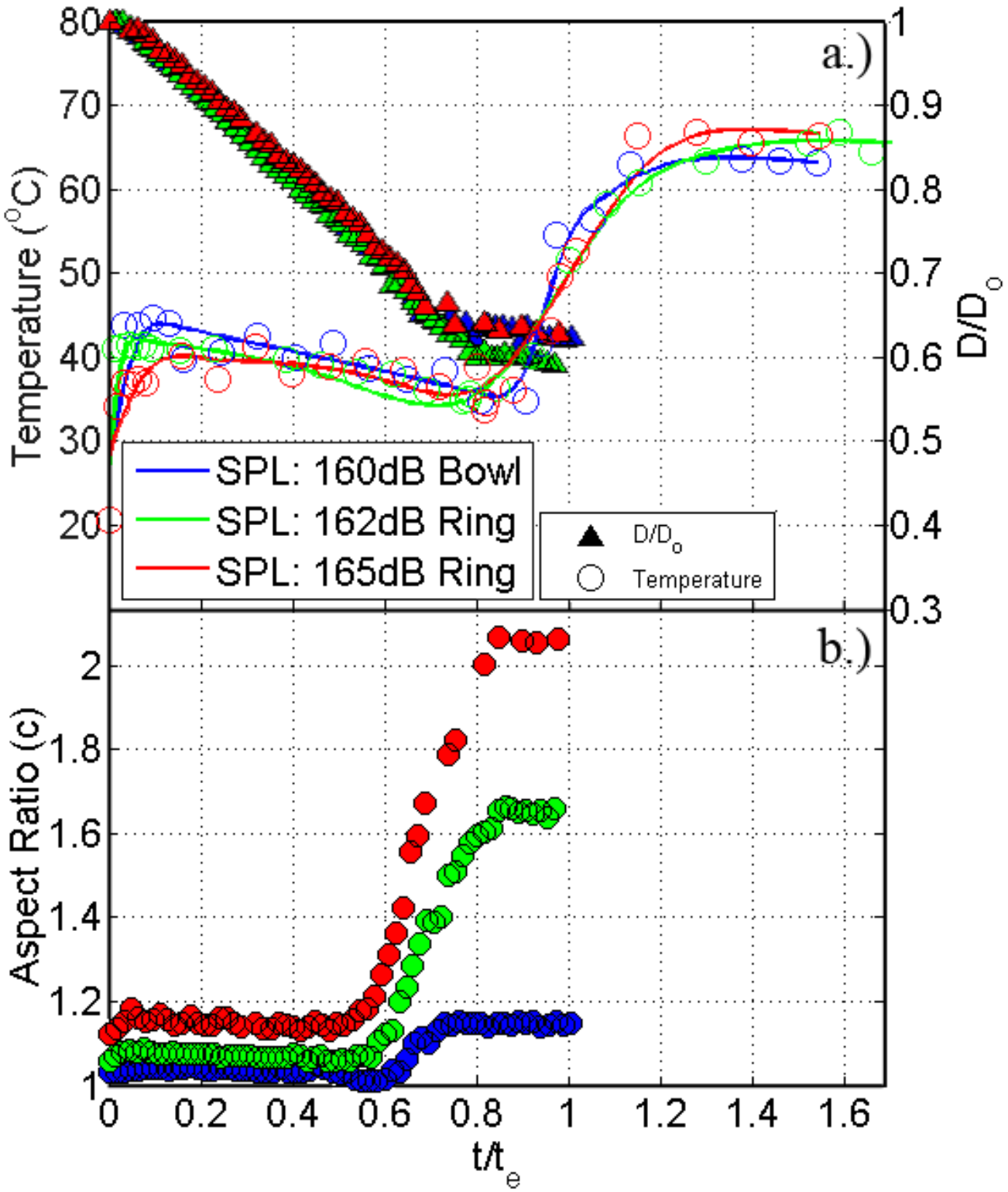

Figure 4.4 a) Surface Temperature and D/Do vs. t/t_e b) Aspect Ratio vs. t/t_e at $\varphi = 2\%$.

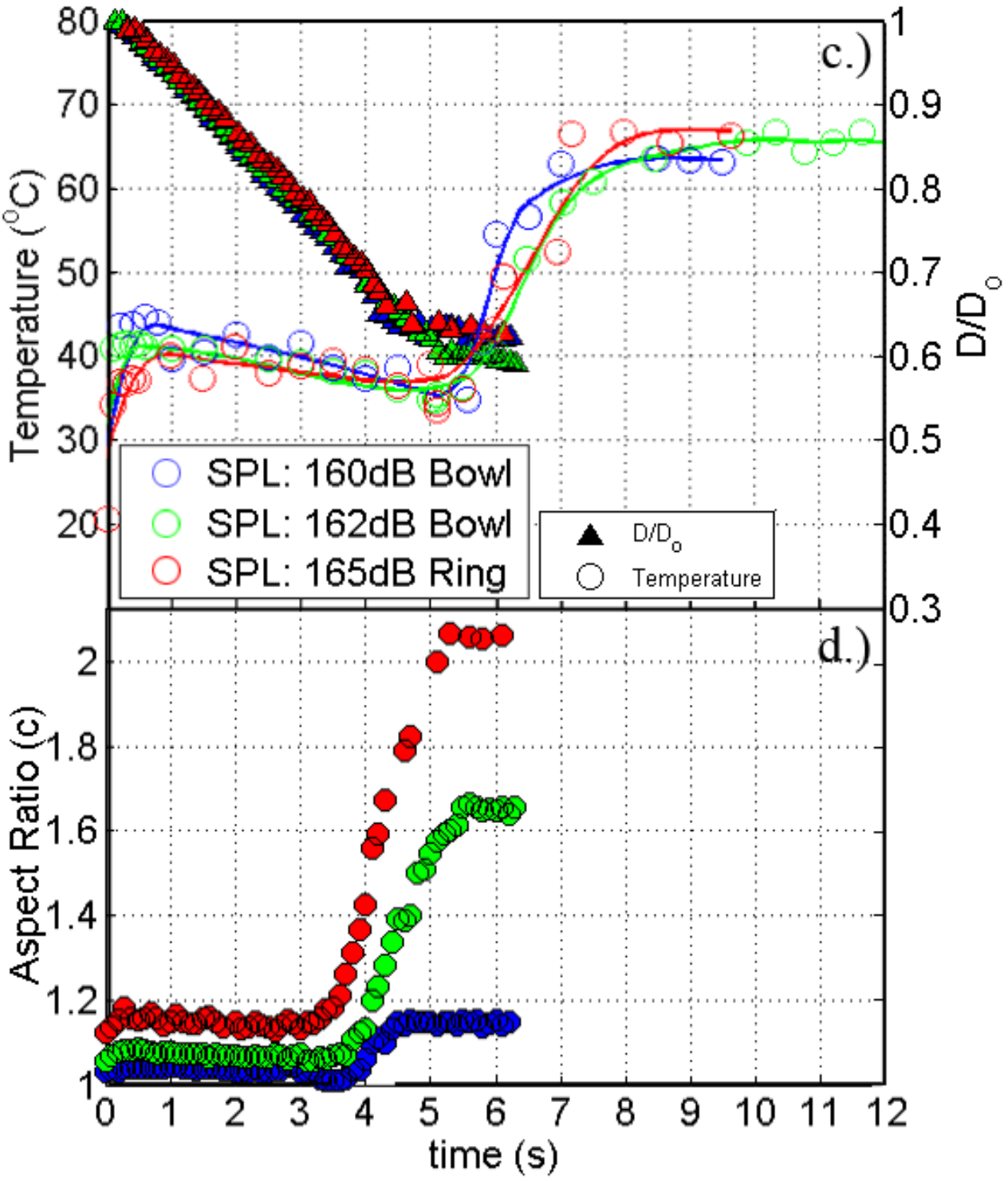

Figure 4.5: c) Surface Temperature and D/Do vs. time d) Aspect Ratio vs. time at φ = 2%.

This leads to a slow decrease in droplet surface temperature. Surface temperature reaches the minimum point when liquid evaporation rate decreases with increase of particle concentration at the droplet surface. Consequently, the heat absorbed from the laser flux raises the temperature of the structure abruptly (second inflection point in Figures 4.2a, 4.4a). The maximum temperature attained by this structure is a weak function of the aspect ratio. Usually there is a decrease of available projected area for heating as aspect ratio increases with increase in SPL (Figures 4.2b, 4.4b). The maximum temperature of the $\varphi = 2\%$ silica solutions is larger compared to the $\varphi = 0.5\%$ due to larger exposed heating area since rings formed at this particle concentration reorient (from horizontal to vertical plane). Structure reorientation can be attributed to non-uniform agglomeration. Non-uniform agglomeration can have two effects on the stability of the structure within the acoustic field, a shift of the structure center of gravity away from the pressure node in the radial direction and asymmetric structure formation. The shift of the center of gravity away from the pressure node causes the acoustic levitation force and the weight of the droplet to become unaligned, since the forces are no longer collinear in this case, an unbalanced torque pair acting on the structure causes it to become unstable and structure rotation occurs. Geometrical asymmetries affect the force acting on different regions on the ring surface; the force applied by the acoustic field is dependent on the geometry of the object perturbing the acoustic field, then the net force acting on one side of the ring can be different than the force acting on the other side of the ring if these are not symmetric. This yields an unbalanced force pair that causes the structure to rotate. Figure 4.6 presents a free body diagram showing the interaction of these forces on the agglomerated ring structure.

In contrast, with the φ = 0.5% cases at 160 and 162dB, the structure formed at a higher SPL has a larger aspect ratio, therefore, the area exposed to heating is smaller, which yields a lower final surface temperature. The diameter reaches a constant value marking the formation of the agglomerated particle structure at different concentrations and different SPL (Figures 4.2a and 4.4a). Aspect ratio also reaches a constant value at the end of the evaporation phase.

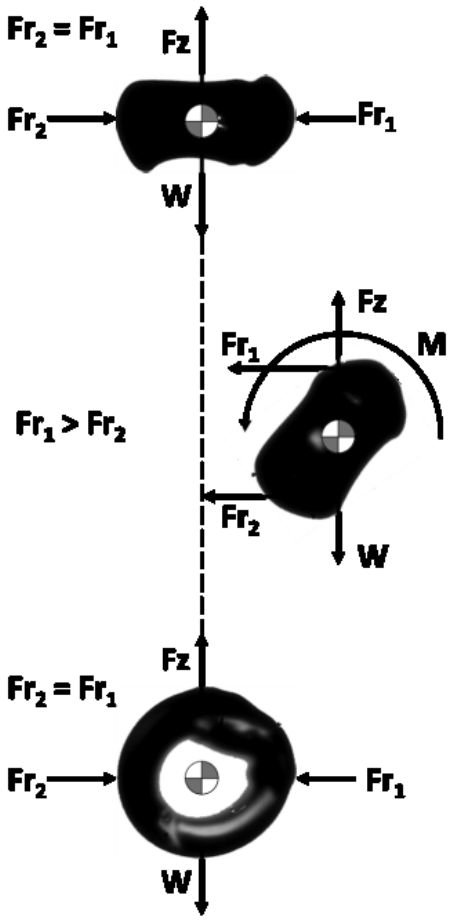

Figure 4.6: Free body diagram.

Figures 4.3c and 4.4c present D/D_o and Temperature vs. time plots, which clearly show that the total time before structure formation varies between 5-8 secs. The droplets with higher initial concentration of nanosilica (Fig. 4.4c) exhibit structure formation relatively faster

compared to the droplets with low initial concentration (Figure 4.3c). Similarly Figures 4.3d and 4.4d represent the temporal variation of aspect ratio (c). The sharp increase in aspect ratio coincides with the inflection point of the diameter regression plots (Figures 4.3c and 4.4c).

Timescales of Vaporization and Agglomeration

As shown in our group's earlier work [15], the timescale for pure evaporation stage is smaller for higher concentration since the amount of solvent to be vaporized is less. Higher solute concentration also suppresses the vapor pressure according to Raoults' law (see Equilibrium of Multiphase Multicomponent Systems in Chapter 2), slowing down the vaporization rate. The total time of the droplet lifecycle (vaporization and agglomeration) is normalized by the evaporation time scale, t_e, which is the time required to evaporate the liquid phase in the droplet. The evaporation timescale is composed of two parts. One part corresponds to the structure formation time t_f which is determined by the time taken by the droplet to form a rigid structure with no further decrease in size. Beyond t_f, evaporation continues as the liquid phase is still present within the structure although no further surface regression is detected. The volume of this residual liquid is calculated by subtracting the volume at the time of structure formation (V_f) from the initial liquid volume (V_o). Finally one can write the evaporation time scale t_e as

$$t_e = t_f + \frac{V_o - V_f}{\dot{V}_f} \tag{4.1}$$

Where $\dot{V}_f$ is the liquid evaporation rate at the instant of structure formation.

Structural Morphology

The nanosilica particles in the droplet are transported by internal recirculation induced by acoustic streaming. As the liquid phase evaporates, the particle concentration near the droplet surface increases, and generates a concentration gradient inside the droplet. Solution viscosity increases with particle concentration [10-14], thus the radial increase in concentration yields a radial increase in viscosity. The fluid momentum is dissipated in the vicinity of the highly viscous droplet surface. Ultimately, agglomeration is triggered near the surface leading to the formation of a shell shaped structure. Figure 4.7 illustrates the particle concentration gradient formation as the liquid phase evaporates, particles agglomerate near the surface causing a depletion of particles in the center region of the droplet giving the resultant structures their shell shaped morphologies. A cross section of a ring structure can be seen Figure 4.8b where this shell geometry is clearly depicted.

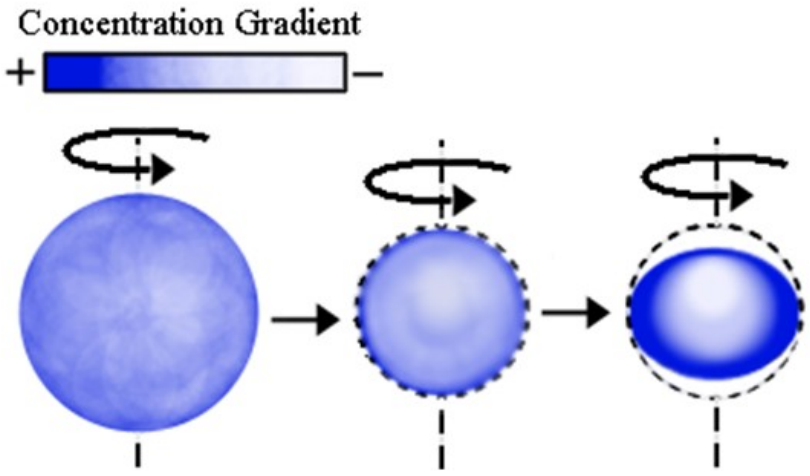

Figure 4.7: Concentration gradient inside the droplet as liquid evaporates.

The microscopic images show that the particles agglomerate into a semisolid lattice i.e. a gel morphology. Structure formation is a consequence of the particle agglomeration, and the rate at which the particles agglomerate into a gel is a determining factor on the structure final dimensions. The different structures (Figure 4.8) exhibit thin to thick shell type features though the overall shape may resemble a bowl, apple-like spheroid or a ring [10]. The final geometry of the structure is not only a function of particle concentration but also of the flow dynamics, evaporation and agglomeration characteristics.

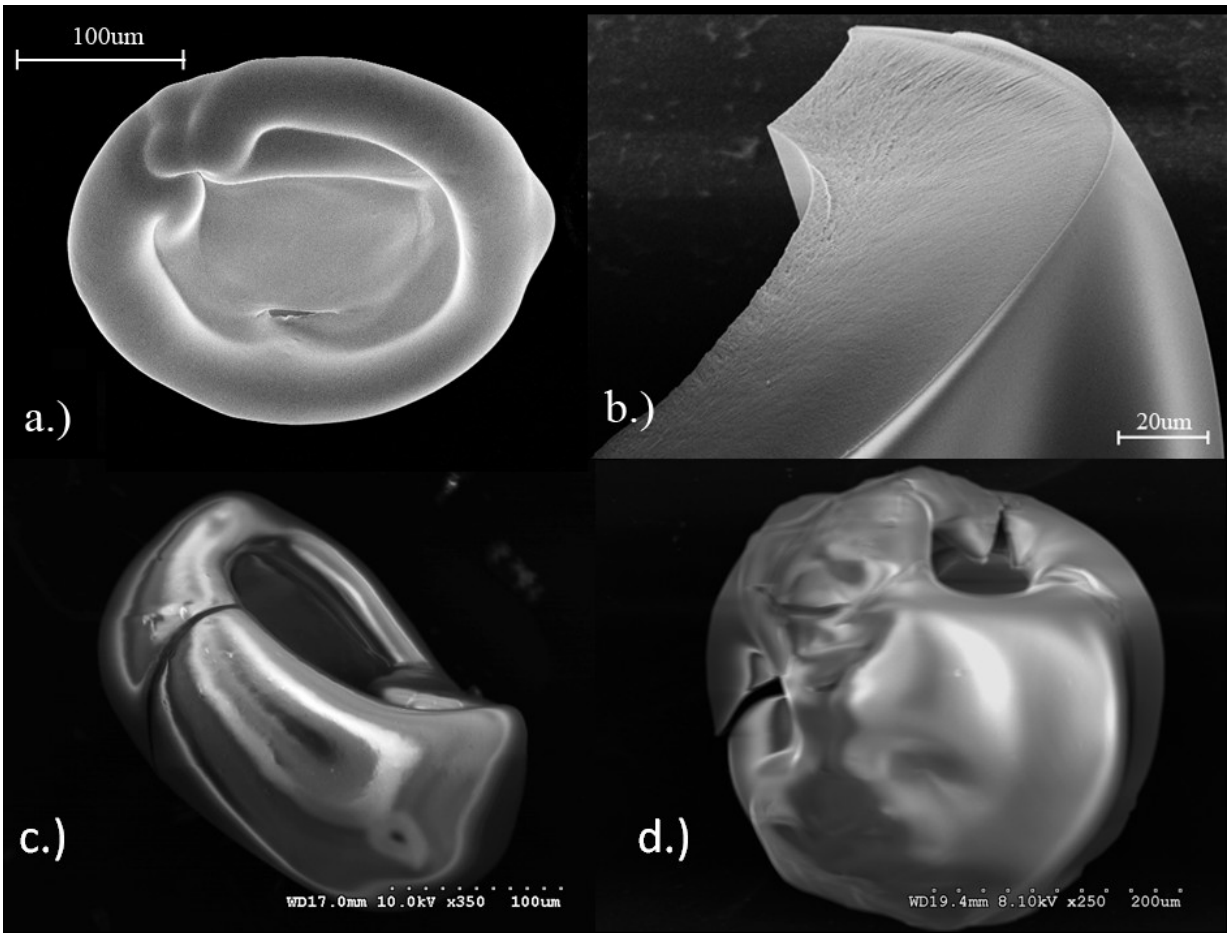

Figure 4.8: SEM images of different structure morphologies. a) 10nm Silica ϕ = 0.5% bowl b) 10nm Silica φ = 2% ring section c) 10nm Silica φ = 2% ring d) 10nm Silica φ =7.33% spheroid.

Evaporation rate governs the rate at which the concentration increases, and is a major contributor in determining the structure geometry. Since recirculation velocity (function of both viscosity and sound pressure level) decreases with viscosity, the particle migration is affected by it. Agglomeration occurs when particles collide due to bulk motion in the droplet. This orthokinetic agglomeration mechanism is a hydrodynamic driven process, and has no dependence on particle size and is a function of particle concentration and flow shear rate. In short, the rate at which the particles migrate to the droplet surface is a function of viscosity which at any time during the evaporation phase is determined by particle concentration, which in turn, changes with the liquid phase evaporation rate.

Agglomeration Time Scale

The effects of evaporation and agglomeration rates are strongly coupled based on the initial concentration and determine the final morphology of the precipitated droplet. The effect of each mechanism, i.e., evaporation rate and agglomeration rate, can be compared by using appropriate time scales. In addition to t_e in equation (4.1), an orthokinetic time scale may be defined as the time required for particles to agglomerate into a gel. In order to calculate the gel agglomeration scale [16], assumptions such as fractal agglomeration and particle monodispersity are taken into account. The time scale for the start of gel formation is defined as [16]:

$$t_g = \frac{\pi D}{4\dot{\gamma}(3-D)}\left(\varphi_o^{-1} - 1\right) \tag{4.2}$$

Where D is fractal dimensionality [35], φ_o is the initial particle concentration and $\dot{\gamma}$ is shear rate or the velocity gradient in the radial direction defined as:

$$\dot{\gamma} = \frac{u_l}{r_d};\ u_l = \sqrt{\frac{\mu_o \rho_o}{\mu_l \rho_l}} u_{max} \tag{4.3}$$

Where r_d is the droplet radius and u_l is the liquid phase velocity scale [5]. Subscripts "*o*" and "*l*" denote the gas and liquid phases respectively. u_{max} is the maximum velocity in the acoustic field, $u_{max} = Mac_o$, where c_o is the speed of sound in the gas phase and Ma is the mach number of the acoustic field related to sound pressure level (SPL) as given by

$$SPL = 197 + 20\log(Ma) \tag{4.4}$$

The orthokinetic time scale (t_g) is therefore a function of fractal dimensionality, initial particle concentration, sound pressure level, viscosities of the liquid and gas phase, density of the liquid phase and droplet size. A control experiment was conducted using 20nm Silica particles to study the effect of particle size on agglomeration; Figures 4.9a and b present a comparison of diameter reduction between 0.5% and 2%vol particle concentration solutions. Droplet diameter vs. time plots are shown in figure 4.9a, the time at which the droplet diameter becomes constant is similar for both 10nm and 20nm solutions. This supports the assumption that the agglomeration time scale does not have a strong dependence on particle size. The same trend can be seen in the normalized diameter plots in Figure 4.9b. The final D/Do values are a function of the droplet agglomeration and deformation scales.

Bulk agglomeration occurs in nanosilica solutions due to strong shear and thermal fields. This has been proven in other systems (not using droplets) by Bremer et al [16] and Kumar et al [10-11]. The timescale for agglomeration is an order of magnitude estimate, and remains unaltered even if evaporation induced enhancement of concentration of nanosilica at the droplet

surface and colloidal repulsive forces influence the actual agglomeration time. Hence using such a timescale is appropriate for the agglomeration process within the droplet.

Since the SPL level is strong enough to induce a surface velocity in the liquid phase of the order of 1-20 cm/sec (see our PIV measurements in 500 μm droplets [21]). This recirculation strongly influences the particle transport and shear rate and hence controls the agglomeration in addition to the thermal field created by radiative heating. It can be seen that the agglomeration timescale decreases with increase in liquid phase velocity. The liquid velocity can be augmented in two ways: by decreasing the viscosity of the liquid phase or by increasing SPL. So the agglomeration timescale is considerably shorter for low viscosity fluids subjected to high SPL.

Evaporation timescale on the other hand depends on the initial particle concentration, sound pressure level and liquid viscosities. High initial particle concentration retards the vaporization rate leading to a longer evaporation timescale. Similarly high SPL leads to increased recirculation velocity inside the droplet which leads to enhanced vaporization, effectively reducing the diffusion length by almost three times. Low viscosity fluids also lead to strong recirculation that further enhances vaporization.

From Equations (4.2) and (4.3), $t_g \sim \sqrt{\mu_l}$, implying that orthokinetic timescale increases with solution viscosity. Evaporation time scale (t_e) is also affected by solution viscosity. Typically the heat transfer inside the droplet scales with the recirculation velocity ($\sim u_l$) which is affected by solution viscosity. Therefore,

$$t_e \sim \frac{1}{u_l} \sim \sqrt{\mu_l} \tag{4.5}$$

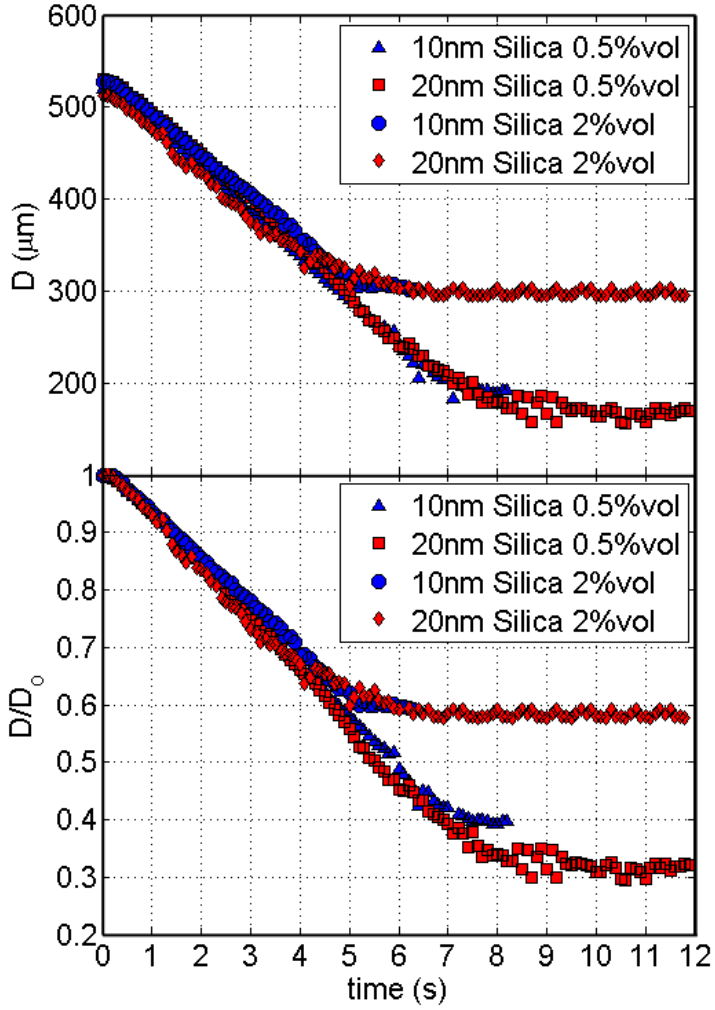

Figure 4.9: a.) Non-dimensional droplet diameter (D/D_o) in time b.) Droplet diameter (D) in time.

A change in viscosity therefore has similar effects on t_e and t_g. This suggests that the ratio, t_g/t_e has a low sensitivity to a change in solution viscosity. Similarly, for a change in SPL,

$$t_g \sim \frac{1}{\dot{\gamma}} \sim \frac{1}{u_l} \tag{4.6}$$

From Equation 4.4,

$$u_l \sim u_{max} \sim Ma\, c_o \sim c_o e^{(SPL-197)/20} \tag{4.7}$$

Finally,

$$t_g \sim \frac{1}{C_o e^{(SPL-197)/20}} \tag{4.8}$$

t_g decreases by a factor of 1.3 for an increase in SPL from 160 db to 165 db. SPL directly influences the recirculation velocity, which affects the evaporation scale by reducing the diffusion distance by a factor of 2. The evaporation timescale thus reduces with increase in acoustic streaming in a similar way as the orthokinetic timescale. Thus, the ratio t_g/t_e has relatively lower sensitivity to SPL.

Finally, initial particle concentration also has a large effect on both t_g and t_e. From Equation 4.2, t_g scales with particle concentration as $t_g \sim \frac{1}{\varphi}$ which signifies that orthokinetic time scale decreases with particle concentration (since the distance between particles decreases with particle concentration). The frequency of particle collisions increases, causing an increase in agglomeration rate. On the contrary, evaporation time calculated based on the initial volume of the liquid in the droplet (in the absence of agglomeration) should decrease with increase in initial particle concentration mainly due to the resistance offered by the surface accumulation of the nanoparticles.

$$t_e \sim \frac{1}{m_{vaporization}} \sim [ln(1+B_m)]^{-1} = 1/\left[ln\left(\frac{1}{1-Y_{v,s}}\right)\right];\ Y_{v,s} \sim p_{v,s} \sim (\varphi p_{sat}) \tag{4.9}$$

Where $Y_{v,s}$ and $p_{v,s}$ are the vapor mass fraction and vapor pressure at the droplet surface and φ signifies initial concentration of the nanoparticles. Thus, t_e will increase with increase in initial particle concentration. This functional dependence of t_e on initial concentration is

opposite to the orthokinetic timescale. Hence t_g/t_e ratio will exhibit high sensitivity to initial concentration. t_g/t_e will decrease with increase in initial concentration (Figure 4.10), and the normalized diameter, D/Do, of the final structure scales with the inverse power of t_g/t_e. For small t_g/t_e, particles begin agglomerating faster near the droplet surface even when the diameter of the droplet has not reduced appreciably mainly due to the time required for evaporation being longer than the time required for particle agglomeration. At $t_g/t_e \sim 1$, agglomeration occurs after significant reduction in droplet size due to evaporation. At high concentrations, t_g/t_e is generally low.

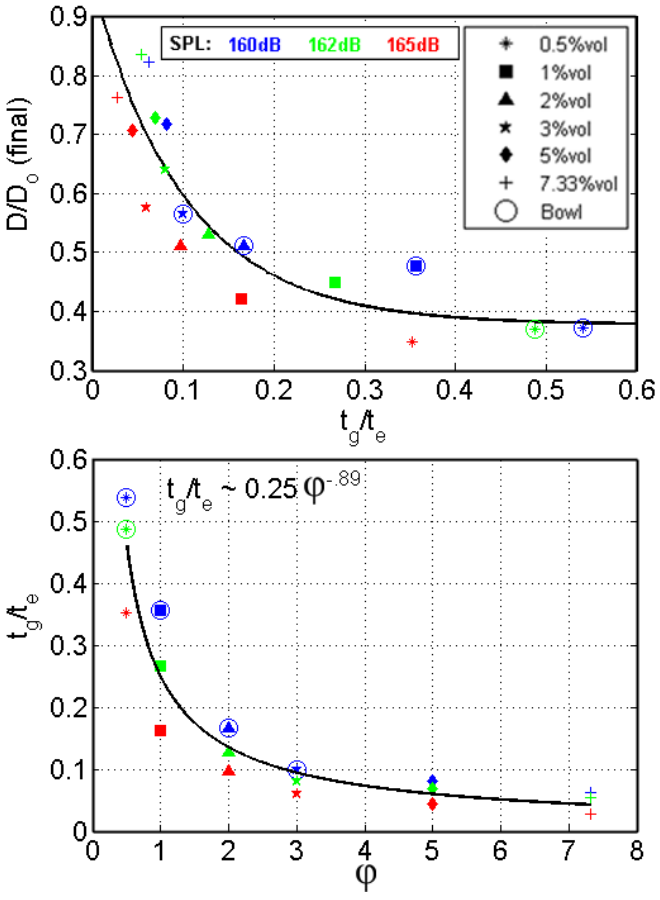

Figure 4.10: Final D/Do with respect to the ratio of orthokinetic time scale (t_g) and liquid phase evaporation time (t_e).

Deformation Timescale

The final structures formed by the droplets exhibit a variety of morphological shapes varying from bowls to rings. These structures can be differentiated from each other based on their aspect ratios. Hence it is clearly understood that the droplets deform considerably due to the acoustic force during the vaporization and agglomeration process. For a droplet at equilibrium, the acoustic pressure force acting on it has to be balanced by surface tension forces. Acoustic pressure is a function of SPL and the magnitude of Laplace pressure is inversely proportional to the interface curvature which in turn is inversely proportional to aspect ratio. The Laplace pressure and RMS value of the acoustic pressure are of similar magnitude prior to precipitation (inflection point of the D/D_0 plot, Figure 4.2 a).

The structure morphology is sensitive to sound pressure level due to the effects SPL has on droplet aspect ratio and on the magnitude of droplet internal recirculation. The droplet aspect ratio increases with acoustic pressure (P_B), an increase in SPL from 160dB to 162dB increases P_B by a factor of ~1.6, similarly an increase from 160dB to 165dB increases P_B by a factor of ~3.2. The recirculation velocity scale (u_l) also increases with SPL, an increase in SPL from 160dB to 162dB increases u_l by a factor of ~1.3, similarly an increase from 160dB to 165dB increases u_l by a factor of ~1.8. Then SPL has a large effect on the structure precursor droplet aspect ratio and on the droplet internal flow which in turn contribute to determine the structure final morphology.

The aspect ratio should ideally increase with increase in SPL in order to balance the additional acoustic pressure force acting on the droplet surface that may lead to droplet

disintegration. As aspect ratio increases, the droplet minor axis length decreases (considering the droplet to be elliptical). The temporal variation of the minor axis of the droplet can be scaled as (neglecting surface tension and viscosity)

$$m_i \frac{d^2y}{dt^2} \sim P_{Acoustic} A_{droplet} \tag{4.10}$$

Where y is the deformation length scale, corresponding to a variation in droplet minor axis length.. The ideal time scale for droplet deformation (t_{def}) is derived by integrating Equation 4.7, yielding

$$t_{def} \equiv \left[\frac{y * m_i}{p_B A_d}\right]^{1/2} \tag{4.11}$$

The deformation length scale is defined as $y = r_p$, the polar mass element is defined as $m_i = \frac{1}{3} m_d$ where m_d is the droplet mass, then t_{def} can be expressed as:

$$t_{def} = \frac{1}{3}\left[\frac{\rho_l}{p_B}\right]^{1/2} r_d \tag{4.11.b}$$

The relative magnitudes of the orthokinetic scale (t_g) and deformation time scale (t_{def}) determine the final structure aspect ratio. If $t_{def} < t_g$, particle agglomeration occurs as the droplet has been already deformed substantially by the acoustic field. At this instant, the droplet aspect ratio is already large. When $t_{def} > t_g$, the increase in aspect ratio requires a longer time than the agglomeration process. Consequently, the particles agglomerate while the aspect ratio is still small. Once agglomeration is triggered, the droplet tends to remain undeformed since the surface rigidity is enhanced by the particulate shell (Figure 4.11). For φ < 2 %, the orthokinetic

timescale is comparatively large. This is reflected by the fact that the droplet deforms substantially before agglomeration is triggered resulting in a large aspect ratio structure. On the other hand, for φ > 2%, the orthokinetic timescale is low which leads to faster agglomeration compared to deformation. This yields low aspect ratio structures. Therefore an inflection point is present at φ ~2% which separates high and low aspect ratio structures.

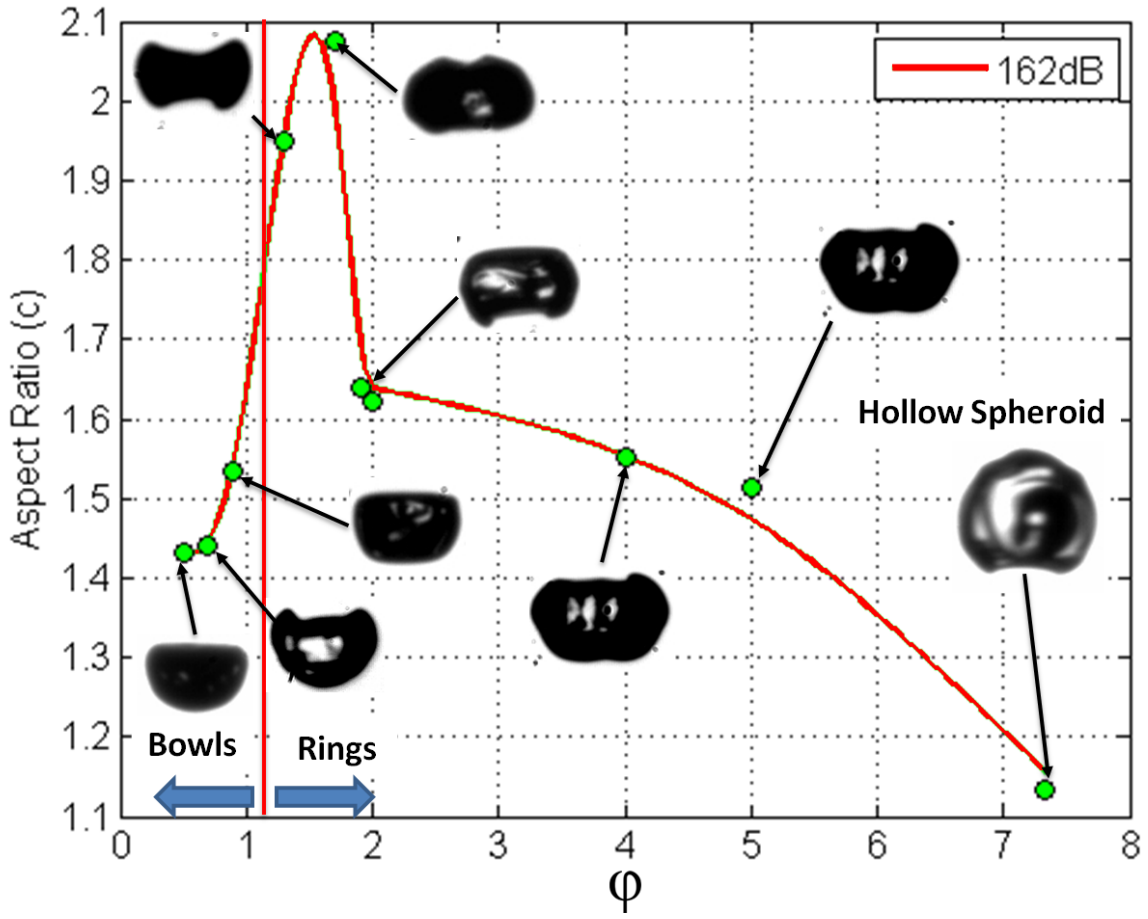

Figure 4.11: Final aspect ratio of the agglomerated structure with respect to initial particle concentration.

Figure 4.12 presents high speed and IR images of the structure formation process of various 10nm Silica solutions. Ring reorientation can been seen in the second and third rows of

images corresponding to 1%vol and 2% vol Silica solutions respectively, the sharp temperature increase associated with ring reorientation can be seen in the infrared images when comparing the structure surface temperature before and after reorientation. This figure also presents the particular case of structure breakup caused by non-uniform particle agglomeration of a 5%vol Silica solution. When breakup occurs the structure fragments are pushed towards the pressure node by the acoustic pressure field (see Acoustic Levitation in Chapter Two).

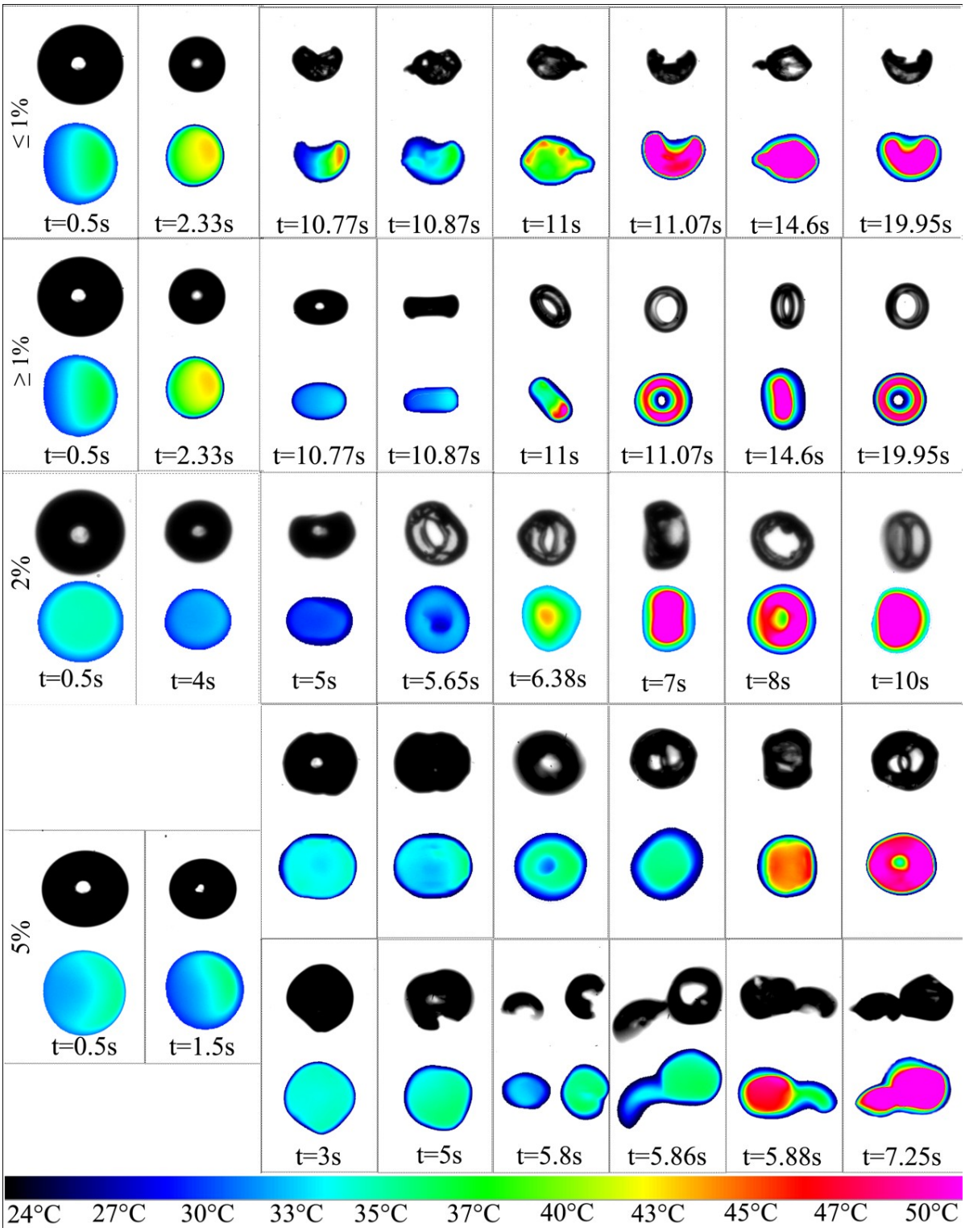

Figure 4.12: Evaporation, structure formation and reorientation for different 10nm Silica solution concentrations.

CHAPTER V: STRUCTURE FORMATION FROM DIFFERENT PRECURSOR SOLUTIONS

The previous chapter presented the process of structure formation by particle agglomeration during the evaporation of the liquid phase in the acoustically levitated droplet. It was shown that the size and geometry of the structure are determined by the outcome of the competition among several mechanisms determined by their timescales: a) evaporation time scale which is the time needed for complete liquid evaporation, b) agglomeration time scale, the time elapsed for particles to agglomerate into a gel by means of orthokinetic agglomeration, and c) the deformation time scale, which is the time needed for droplet to deform.

Both evaporation and agglomeration time scales are functions of sound pressure level (SPL), droplet size, solution viscosity and density. Similarly, the deformation time scale is a function of SPL and solution surface tension. Then the outcome of the structure formation phenomenon can be expressed as a function of the solution properties discussed earlier and it is not dependent on the particle size or type. The relationship between particle size and concentration with solution viscosity and surface tension have been studied by others [4, 36, 37], this is beyond the scope of this study. This analysis is done by directly measuring the solution properties to characterize each solution's agglomeration and evaporation time scales as well as the droplet acoustic interactions that cause deformation. Experiments utilizing different solutions, 10 and 20nm Silica as well as 20 and 50nm Alumina, were conducted to compare how well the time scale model holds for different solutions. In addition, the viscosity and surface

tension of 10 and 20nm Silica solutions have been altered by adding glycerin and surfactant in order to evaluate the impact of property changes on structure formation.

Solution Properties

Viscosity and surface tension of the different Silica and Alumina solutions used in this study were measured at different particle concentrations. Solution viscosity "μ_l" increases with particle concentration, shown in figure 5.1a. In this figure it can be seen that the 50nm Alumina solutions have higher viscosities in the 0.5 to 5%vol particle concentration range, this has a direct impact on structure formation due to the magnitude of agglomeration time scale "t_g" for these solutions. Similarly surface tension of the Silica and Alumina solutions were measured at different concentrations. Solution surface tension "σ" decreases with particle concentration. In the special case of the 20nm Alumina solutions the dispersing agent in the solution, used to maintain stable colloidal suspension, causes a noticeable sharp decrease in surface tension decrease with particle concentration due to the larger solution volume containing the dispersing agent needed to increase particle concentration. Figure 5.1b presents σ with respect to particle concentration "φ".

Figure 5.2a presents the temperature dependence of φ = 0.5% 50nm Alumina solution viscosity, similarly figure 5.2b presents the temperature dependence of φ = 0.5% 50nm Alumina solution surface tension. Droplet temperature increases during heating, and as liquid evaporates particle concentration increases, then solution viscosity and surface tension vary during the liquid evaporation phase.

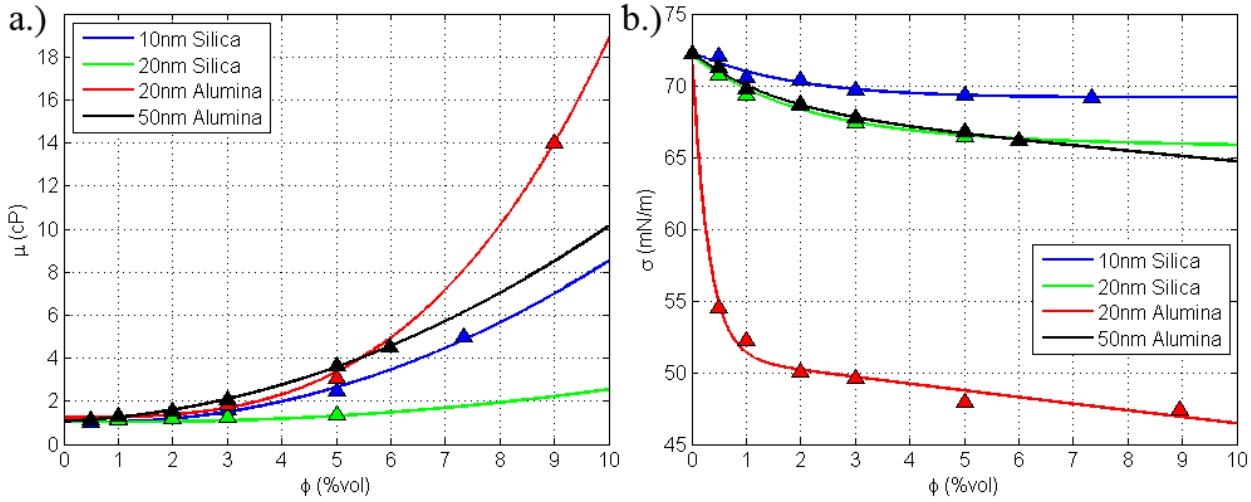

Figure 5.1: a.) Viscosity "μ_l" vs. Particle Concentration "φ" b.) Surface Tension "σ" vs. Particle Concentration "φ"

As particle concentration and droplet temperature vary in time, solution viscosity and surface tension do as well. The sensitivity of solution viscosity to particle concentration is higher than to solution temperature, this can be seen in figures 5.2a and 5.2b.

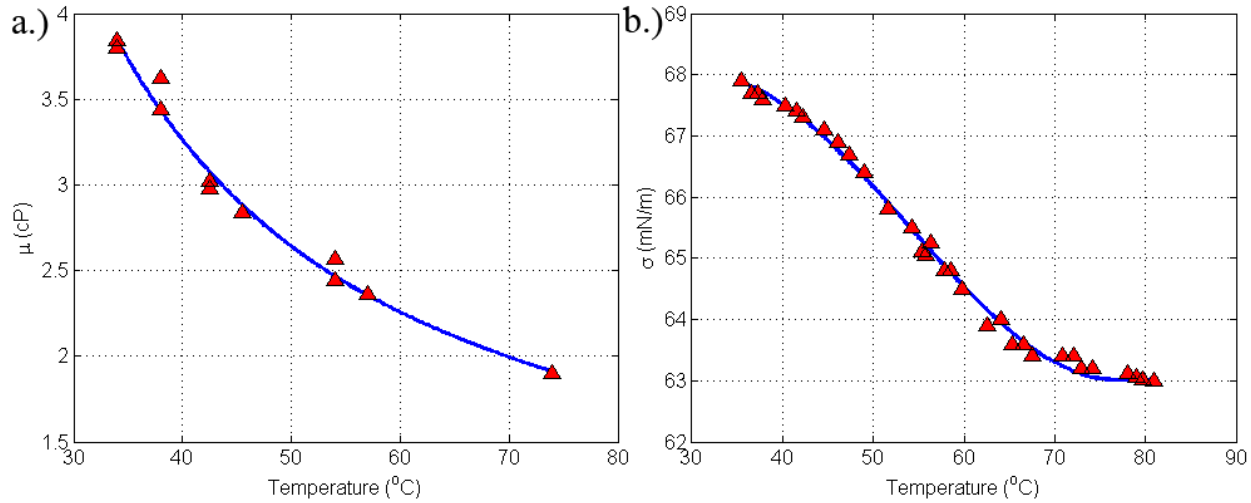

Figure 5.2: a) Viscosity "μ_l" vs. Temperature b.) Surface Tension "σ" vs. Temperature, 50nm Alumina, φ = 5.99%.

The maximum temperature during evaporation of approximately 45°C, decreases the surface tension of φ = 5.99% 50nm Alumina by 25%. An increase in solution concentration from

5.99% to 20% (the final estimated concentration at the time of structure formation t_f) yields a 750% increase in solution viscosity. Then the temperature effect on viscosity can be neglected compared to the viscosity increase caused by the increase in particle concentration. The approximate instantaneous solution viscosity during the experiment can then be estimated by calculating the instantaneous particle concentration in the droplet. Since the particle volume within the droplet is known and remains constant through the experiment, the instantaneous particle concentration can be calculated using the high speed imaging data indicating the instantaneous droplet volume, shown in figure 5.3a. The solution viscosity can be estimated using the measured viscosity dependence on particle concentration shown in figure 5.1. The instantaneous viscosity of φ = 5.99% 50nm Alumina is shown in figure 5.3b.

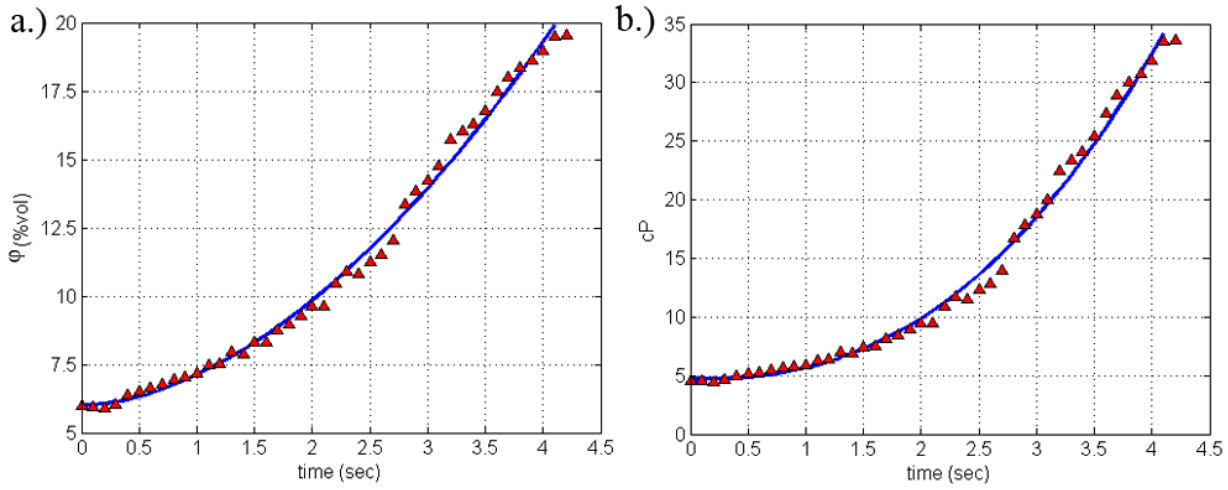

Figure 5.3: a.) Concentration "φ" vs. Time b.) Viscosity "μ_l" vs. Time, 50nm Alumina.

Figure 5.3b illustrates an ideal approximation of the viscosity increase caused by concentration increase in time. But in fact the increase in solution viscosity is not uniform across the droplet, as liquid evaporates at the droplet surface the local viscosity increases. This localized increase in viscosity near the droplet surface yields a velocity gradient in the radial direction. The

velocity of the recirculation flow within the droplet decreases in the radial direction and causes the increase of particle concentration near the surface due to deposition of the particles being carried by the flow, giving the structures their characteristic shell morphology [14, 38]. The droplet surface temperature in time was recorded using infrared imaging in parallel with high speed imaging. From this data the surface temperature is known (figure 5.4a) and by correlating surface tension to temperature, using the measured surface tension with respect to temperature data (figure 5.2b), the instantaneous droplet surface tension can then be calculated (figure 5.4b). Surface tension first decreases sharply with the increase in surface temperature, as the temperature of the droplet decreases with the liquid phase evaporation surface tension decreases. The initial surface tension and the magnitude of this drop determine the length of the deformation time scale which in turn is a determinant in the final structure morphology [38]. The function of surface tension with respect to temperature is not valid after the droplet surface has solidified at t_f, this instant is marked with an "x" on the surface tension curves in figure 5.4b.

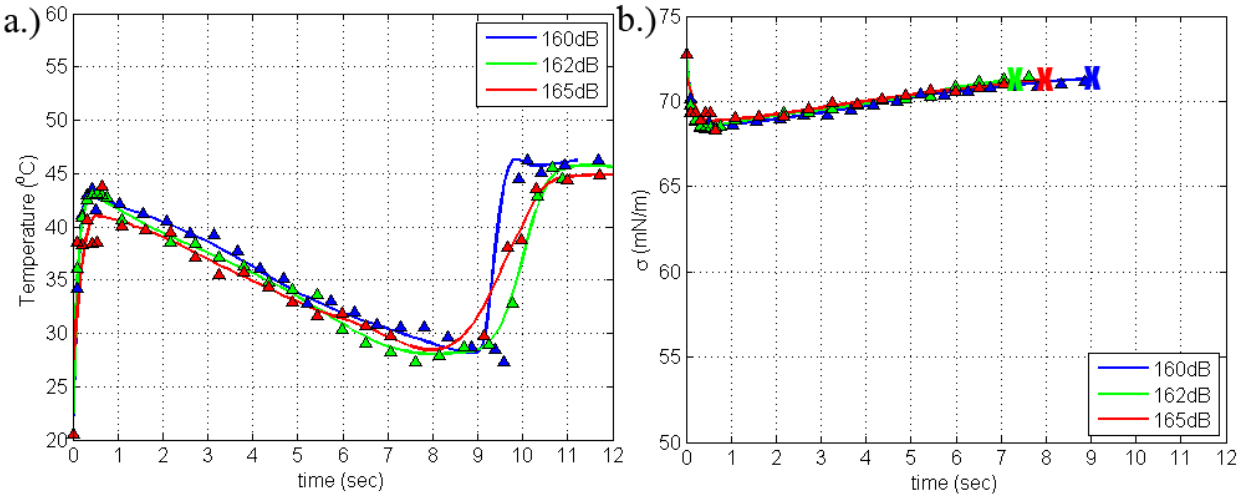

Figure 5.4: a.) φ = 0.5% Temperature vs. time. b) φ = 0.5% Surface Tension "σ" vs. time, 50nm Alumina.

Results

Particles of different types and sized were used in this work, 10nm and 20nm Silica as well as 20nm and 50nm Alumina. Experiments were conducted at particles concentrations of φ = 0.5, 1, 2, 3 and 5%vol, in addition to these, the maximum concentrations attainable from the colloidal suspensions manufacturer (Alpha-Aesar) were also studied. In the case of 10nm Silica the maximum concentration used was φ = 7.33%vol, 20nm Silica φ = 23.11%vol, 20nm Alumina φ = 8.99%vol and 50nm Alumina φ = 5.99%vol. Experiments were conducted with four different types of particles, six particle concentrations and three SPL (160, 162 and 165dB) for each particle type. In addition glycerin was added to 0.5 and 2%vol 10nm Silica solutions (1 and 4%vol glycerin concentrations respectively) to study the effect of solution viscosity increase on structure formation. Similarly, surfactant was added (1%wt) to 10nm and 20nm Silica particle concentration φ = 0.5%vol solutions to observe the effect of surface tension reduction on the final structure morphology.

As presented in the previous chapter, the final structure normalized diameter "D/D_o" is presented as a function of the ratio of agglomeration and evaporation time scales "t_g/t_e". It was proposed that the result of the structure formation process is dependent only on the fluid properties of the solution and the acoustic levitation amplitude (SPL). The characteristic time scales used to correlate the results, are functions of the particular fluid properties and levitation conditions of each sample of the different nanofluid solutions. There is good agreement between the results presented from the work done on 10nm Silica solutions and the results of the work done with different particle solutions; this can be seen in figure 5.5. The resultant structure D/D_o

shows an exponential correlation with t_g/t_e. The different particle and concentration cases, with different fluid properties, correlate well to this exponential curve which supports the proposed concept of characterizing the structure formation phenomenon with the properties of the precursor solutions and the conditions of acoustic levitation using the previously proposed time scale relations. The results from manipulating solution viscosity and surface tension by addition of glycerin and surfactant are also presented in figure 5.5. These special cases also agree well with the rest of the cases, the modification to the solutions' properties affects the structure formation process due to the effect of these properties variations on the magnitude of agglomeration, evaporation and deformation time scales. As result, the change in solution properties affects the final structure morphology.

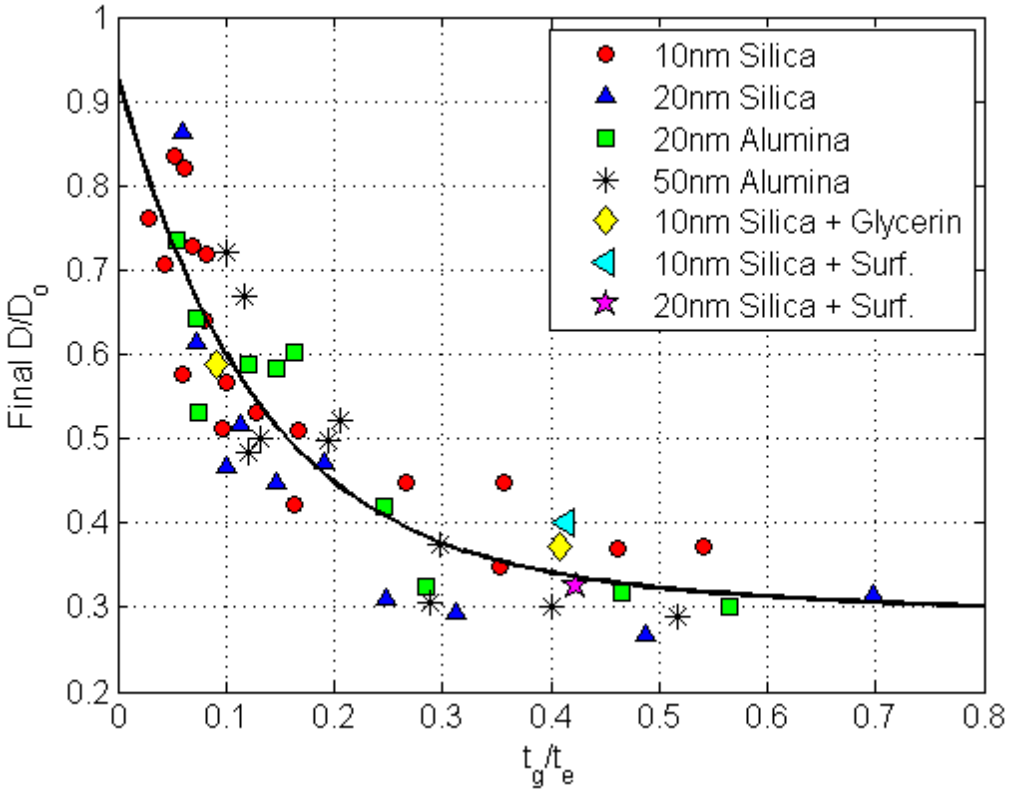

Figure 5.5: Final D/D_o vs. t_g/t_e for different particle solutions.

Glycerin was added (1%vol) to a φ = 0.5% 10nm Silica solution, viscosity increased from 1.04cP to 1.12cP (7.7% increase), a value close to the viscosity of 50nm Alumina φ = 0.5%vol solution of 1.13cP. Glycerin was also added (4%vol) to a 2%vol 10nm Silica solution, the viscosity increased from 1.45cP to 1.53cP (5.5% increase) matching the viscosity of the 50nm Alumina 2%vol solution of 1.53cP. The effect of glycerin addition on vapor pressure has been taken into consideration, an addition of 1%vol Glycerin decreases vapor pressure approximately by 0.34Pa (0.34% decrease) and approximately 1.12Pa (1.1% decrease) for 4% Glycerin concentration [39]. The effect of glycerin addition on the evaporation rate can be neglected due to the small decrease in vapor pressure. The recirculation velocity scale scales with viscosity as $u_l \sim \sqrt{\mu_l}$ (equation 2.5), from equation 4.2 the agglomeration time scale varies with u_l as:

$$t_g \sim \frac{1}{\dot{\gamma}} \sim \frac{1}{u_l} \tag{5.1}$$

then t_g scales with recirculation velocity scale as:

$$t_g \sim \sqrt{\mu_l} \tag{5.2}$$

The reduction on recirculation within the droplet also increases the evaporation time scale t_e due to the decrease of convection within the droplet which hinders the heat transfer from the surface to the center of the droplet. The increase in evaporation time scale manifests as a longer time for structure formation t_f at which both structure D/D_o and aspect ratio have stabilized, this can be seen in figure 5.6.a when comparing the solutions with added glycerin with the untamed 10nm Silica solutions.

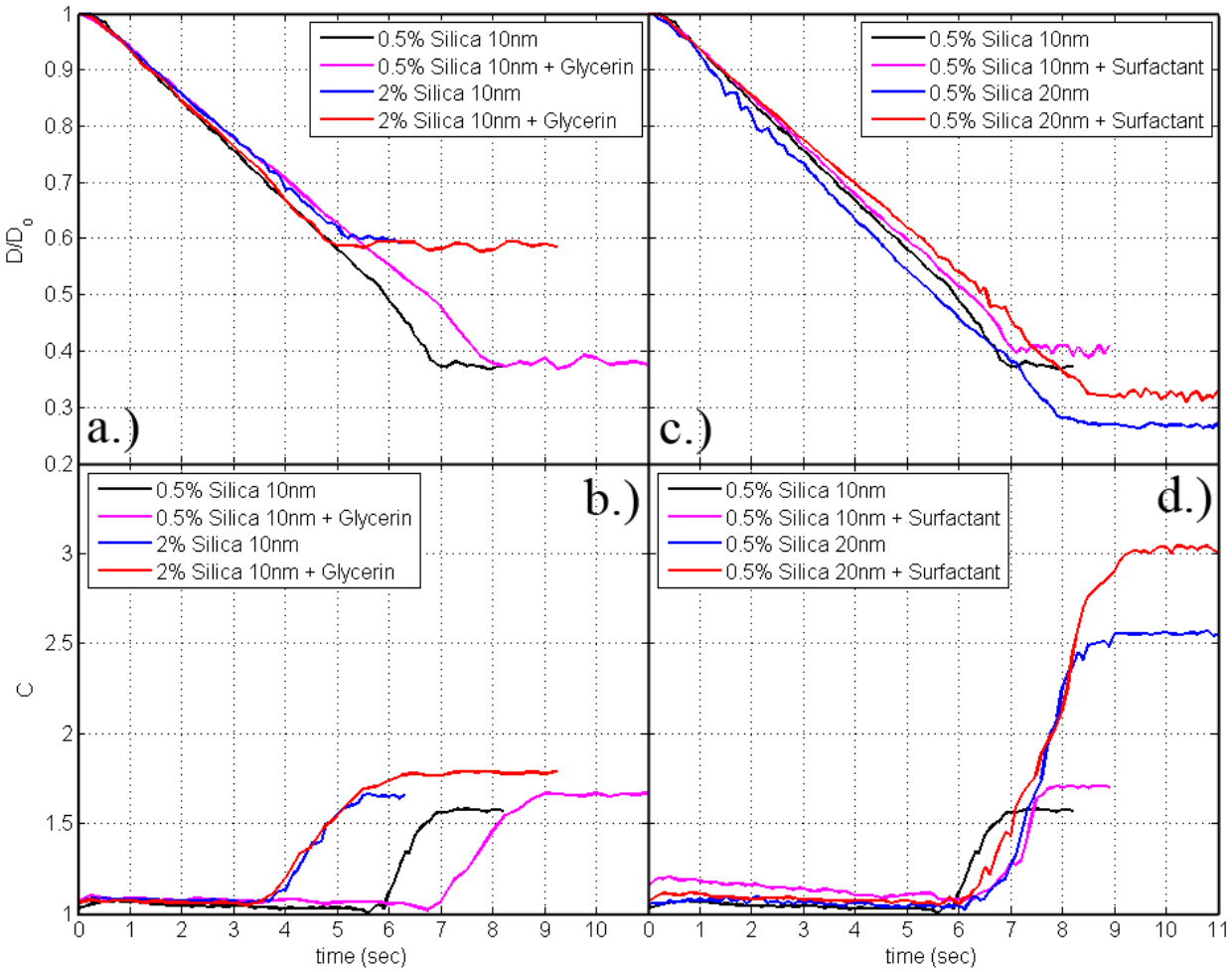

Figure 5.6: a.) D/D_o vs. time b.) Aspect ratio vs. time 10nm Silica ϕ = 0.5%vol, 2% + Glycerin c.) D/D_o vs. time d.) Aspect Ratio vs. time 10nm and 20nm Silica ϕ = 0.5%vol + Surfactant.

The Surface tension of 10nm Silica and 20 nm Silica φ = 0.5%vol were modified by adding "Polisorbate 80" (Alpha-Aesar) surfactant to these solutions at a 1%vol concentration. Surface tension of the 10nm Silica solution was reduced from 72.2 to 53.9mN/m, similarly the surface tension of the 20nm Silica solution decreased from 65.3 to 54.9mN/m. Decreasing solution surface tension increases the droplet aspect ratio (shown in figure 5.6.d), the droplet area exposed to the radiative heat source (CO_2 laser) decreases with aspect ratio. The heat flux from

the radiative heat source is maintained constant then the decrease in droplet heat transfer area causes a reduction in the total heat flow to the droplet. Due to the reduction of heat transferred to the droplet, the evaporation time t_e scale increases, the increase in this time scale can be seen in figure 5.7b when comparing the droplet normalized diameter reduction D/D_o and aspect ratio in time of the solutions containing surfactant to the solutions with no surfactant content.

The increase of t_e with viscosity is of larger magnitude compared to the increase of t_g, subsequently the increase in viscosity has an overall effect of decreasing the ratio of agglomeration and evaporation time scales t_g/t_e. Due to the longer evaporation time scale compared to the agglomeration time scale, particles agglomerate at an instant when the droplet is larger compared to the droplet size at the time of agglomeration of the lower viscosity solutions. This yields a larger final structure size manifested on larger final D/D_o, this agrees well with the trend observed in the previously presented data. Final D/D_o increases exponentially with the decrease of the t_g/t_e ratio. This is shown in figure 5.7.a, as expected both cases move up the correlation curve as t_g/t_e. D/D_o shows a slight increase with the addition of glycerin to 10nm Silica φ = 0.5%vol in contrast with the large increase of D/D_o caused by glycerin addition to 10nm Silica φ = 2%vol, this is consistent to the D/D_o inverse exponential correlation to t_g/t_e.

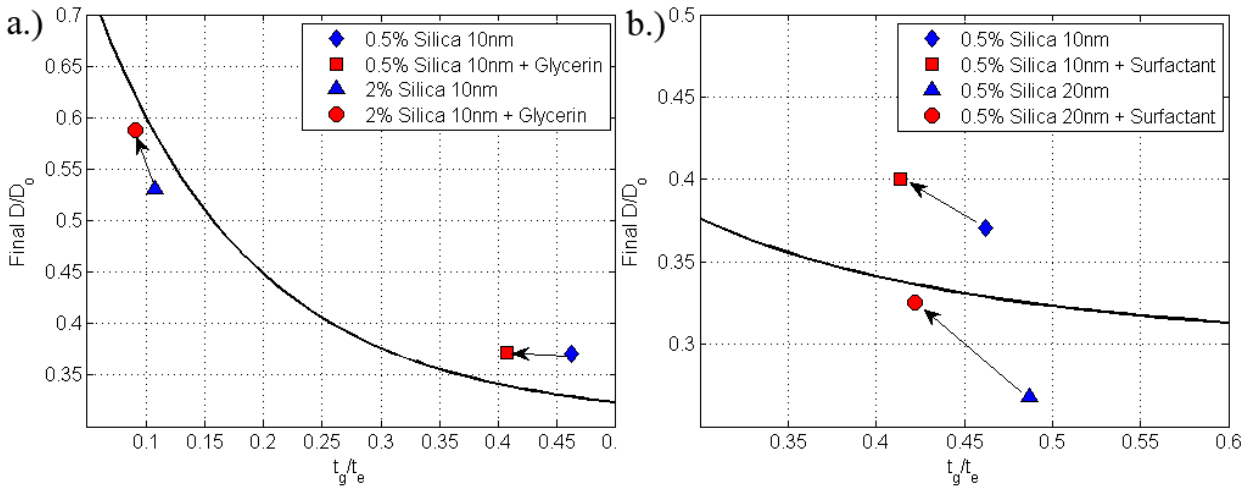

Figure 5.7: D/D_o vs. time a.) 10nm Silica + Glycerin b.) 10nm and 20nm Silica + Surfactant.

Surface tension reduction results in a decrease in agglomeration to evaporation time scale ratio t_g/t_e, similarly to increased viscosity cases, final D/D_o increases with the decrease of t_g/t_e which is consistent with our previous observations. The structure final aspect ratio is also affected by the increase in evaporation time scale caused by increased solution viscosity and reduced surface tension. In the case of viscosity increase the evaporation time scale is larger compared to the deformation time scale yielding larger aspect ratio structures. Figure 5.8 presents a comparison of 10nm Silica with and without added glycerin to 50nm Alumina that has a similar viscosity, a bowl structure forms in the case of no glycerin added (figure 5.8.a) in contrast a ring is formed in the case with added glycerin (figure 5.8.b) which is similar to the ring formed from the 50nm Alumina precursor droplet solution (figure 5.8.d).

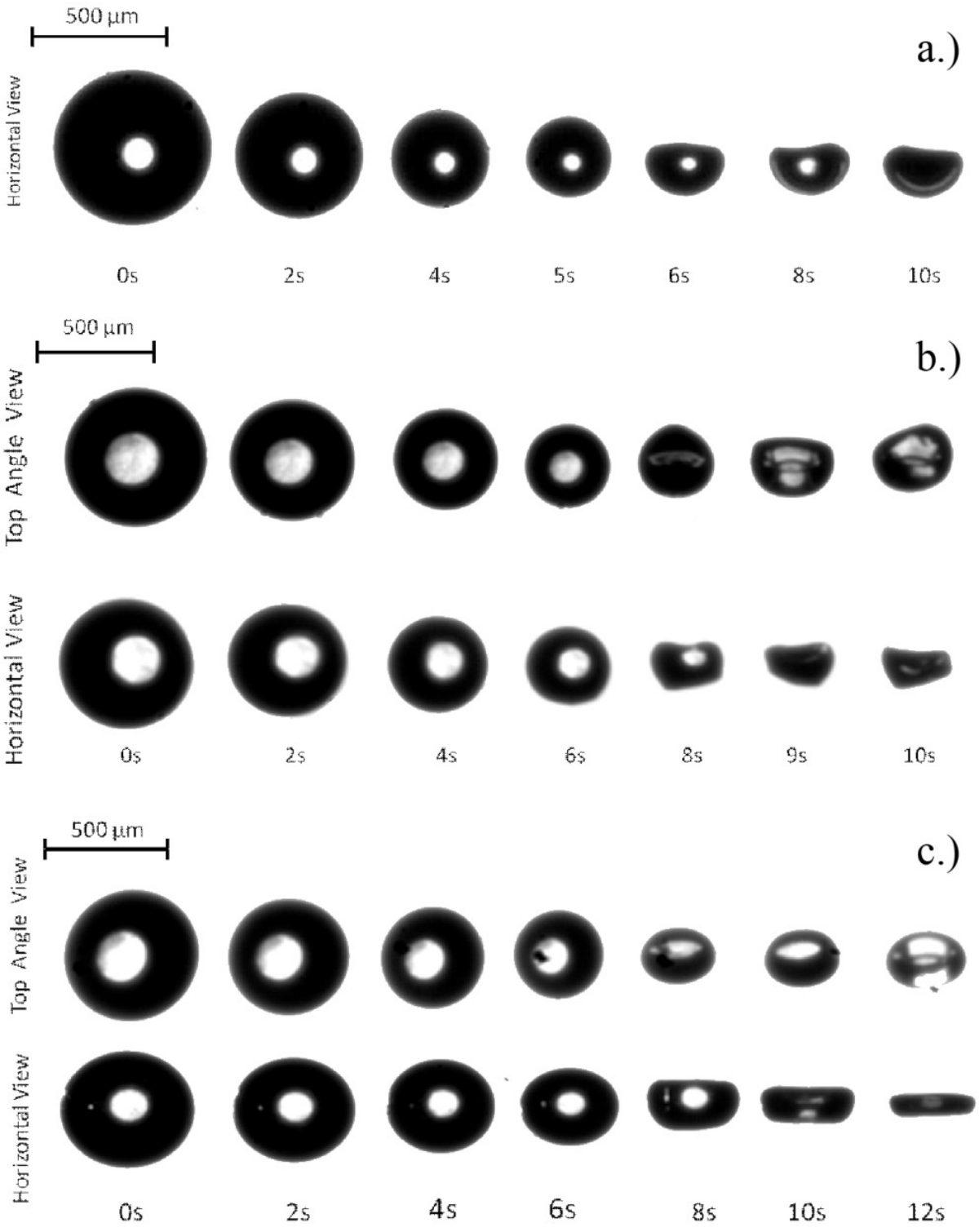

Figure 5.8: a) 10nm Silica b) 10nm Silica + Glycerin, c) 50nm Alumina φ = 0.5%vol.

The deformation time scale is reduced due to the decrease in surface free energy caused by the reduction of surface tension. This yields larger aspect ratio structures due to the increased aspect ratio of the precursor droplets. In addition to the reduction of t_{def} , the evaporation time scale is increased due to the reduction of projected area to heating caused by the increase in aspect ratio, then the deformation time scale magnitude with respect to the evaporation time scale is reduced even further, contributing to the formation of high aspect ratio structures (figure 5.9.b) such as rings. Figure 5.9 presents a comparison between 10nm Silica φ = 0.5%vol with and without added surfactant (figure 5.9.a), bowls are formed in the higher surface tension cases, in contrast, rings are formed in the case of reduced surface tension (figure 5.9.b).

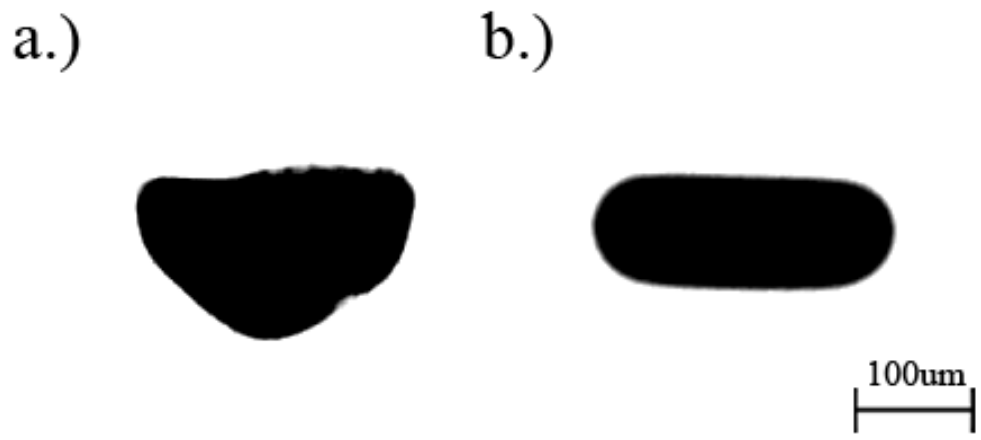

Figure 5.9: a) 10nm Silica b) 10nm Silica + Surfactant, φ = 0.5%vol

A different morphology was observed in the case of 20nm Alumina solutions, these solutions have high viscosity (of comparable to 50nm Alumina, 1.17 to 14cP) and low surface tension (50 to 57mN/m) yielding structures that differ from the bowls and rings observed from 10nm and 20nm Silica and also from 50nm Alumina. The structures formed from these precursor

solutions have disc geometry surrounded by a toroidal edge which differs from the hollow structure geometries observed from the other precursor solutions. This is due to the reduced recirculation within the droplet caused by the solutions high viscosity and the droplets low surface tension. Low recirculation means that the particle migration rate is lower compared to droplets of less viscous solutions and low surface tension yields droplets of higher aspect ratios compared to the higher surface tension droplets. This results in a flat disc shaped geometry, an annulus is formed at the edge of the structure due to centrifugal force induced from droplet rotation along the longitudinal levitation axis caused by secondary acoustic streaming [5, 7-9 , 29, 30]. Figure 5.10 presents Scanning Electron Microscopy (SEM) images from a disc structure formed from 20nm Alumina $\varphi = 0.5\%$vol.

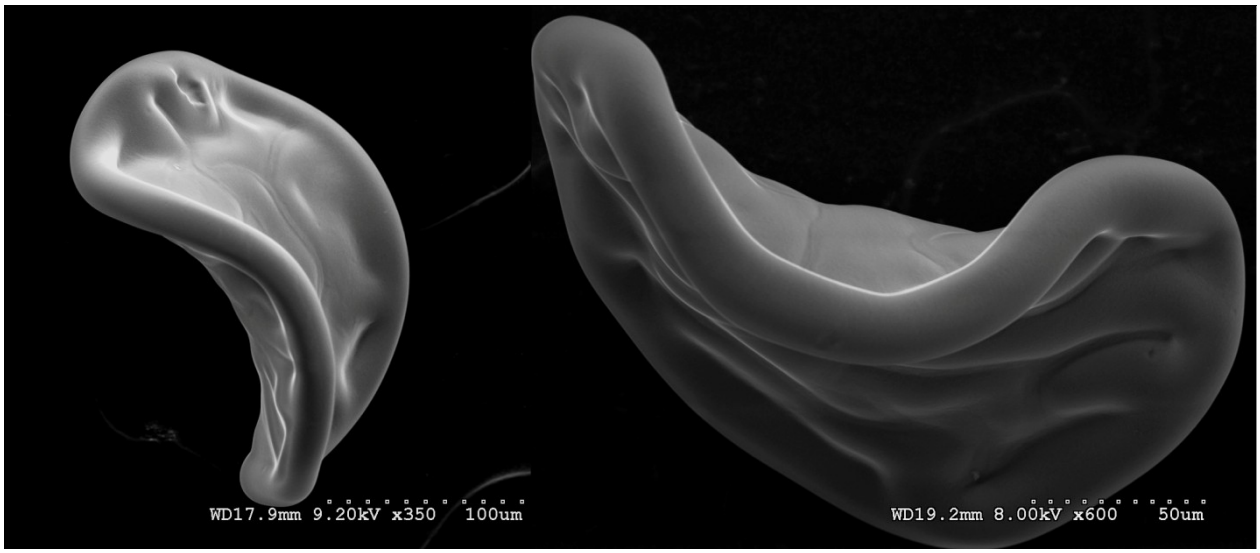

Figure 5.10: SEM images of a disc structure formed from 20nm Alumina 0.5%vol.

These structures have high aspect ratios due to the solutions' low surface tension which decreases the deformation time scale. A comparison between 20nm Silica and 20nm Alumina

final aspect ratio is made in figure 5.11, 20nm Alumina solutions yield structures of higher aspect ratio compared to the structures formed from higher surface tension 20nm Silica solutions.

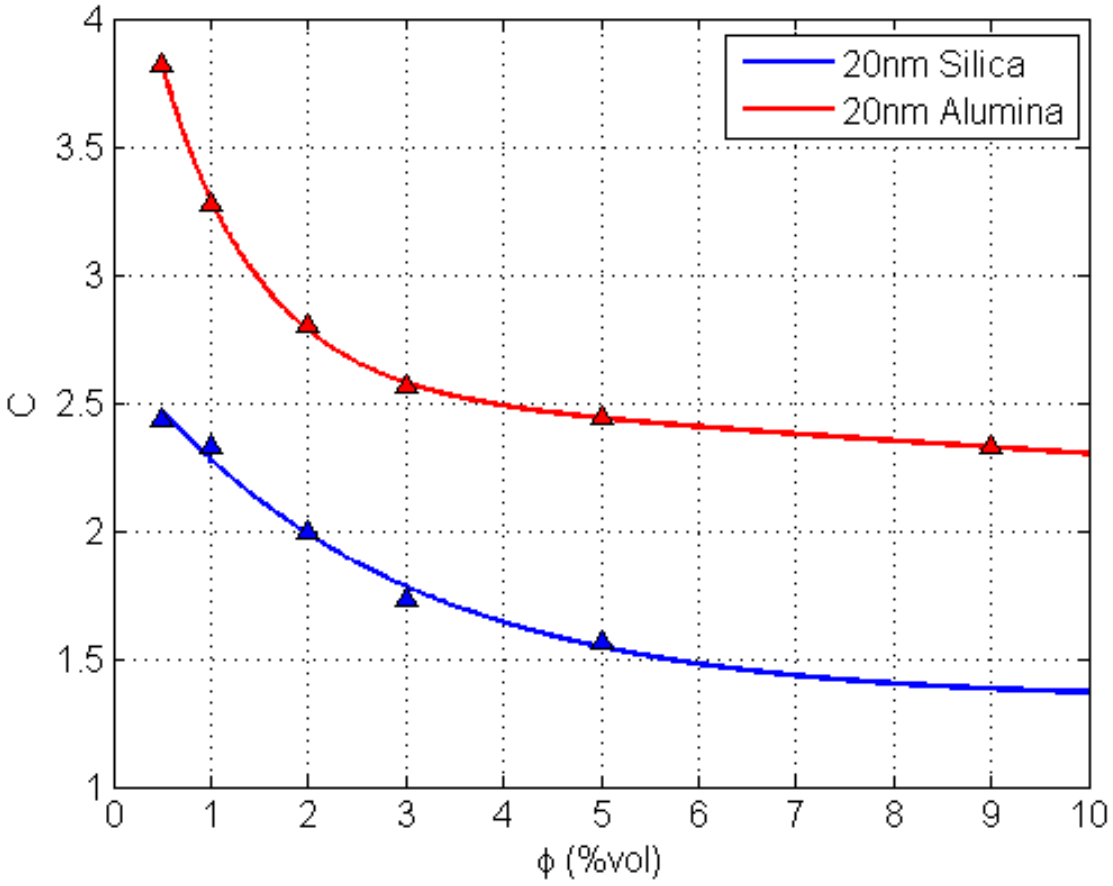

Figure 5.11: Final Aspect Ratio "C" vs. φ, 20nm Silica and 20nm Alumina Solutions.

Time for structure formation "t_f" [38], defined as the time when particles have agglomerated forming an exterior solid shell and after which the exterior surface radial regression stops, decreases with particle concentration. The structure formation phases, evaporation, agglomeration and structure reorientation, are illustrated by phase diagrams [21] for each different nanofluid solution in figure 5.12. The regions in the time-initial particle concentration domain, delimited by the solid lines, represent the distinct phases of the structure

formation process. The region beneath the blue structure formation line corresponds to the liquid phase evaporation phase, recirculation, particle migration and early agglomeration occur during this phase, thus final structure geometry is defined in this phase.

The time for structure formation is not only a function of particle concentration but it is also affected by solution viscosity and surface tension. As stated earlier, recirculation decreases with viscosity which in turn causes a decrease in evaporation rate due to the reduction of convection within the droplet. At a constant heat flux, the droplet heat absorption rate is proportional to the area exposed to heating, this area decreases with aspect ratio which in turn increases with a decrease in surface tension. Thus the time for structure formation increases with viscosity and increases with decreasing surface tension. These effects can be seen in figure 5.12 when comparing the different cases to each other. Figure 5.12.a presents the phase diagram for 10nm Silica solutions. When compared to the 20nm Silica solutions phase diagram (5.12.b), it can be noted that the evaporation phase is longer in the cases of the 20nm Silica solutions. Even though the viscosity of the later solutions is lower, especially at concentrations higher than 3%vol, the effect on evaporation rate caused by lower surface tension is dominant thus increasing "t_f". The 20nm Alumina cases, figure 5.12.c, present the extreme effects of high viscosity and low surface tension, this results in liquid evaporation rate reduction and a longer structure formation time compared to high viscosity 50nm Alumina (figure 5.12.d).

Structure reorientation of ring structures formed at solution concentrations higher than φ = 1%vol was observed in the cases of 10nm and 20nm Silica caused by geometric asymmetries due to non-uniform particle agglomeration [14, 38]. The time at which this happens is depicted

by red lines in figures 5.12.a and b. The area between the structure reorientation and structure formation lines represents the region at which the interior of the structures is at the final stage of agglomeration thus the internal geometry is still changing, these mass swifts within the structure ultimately cause structure reorientation.

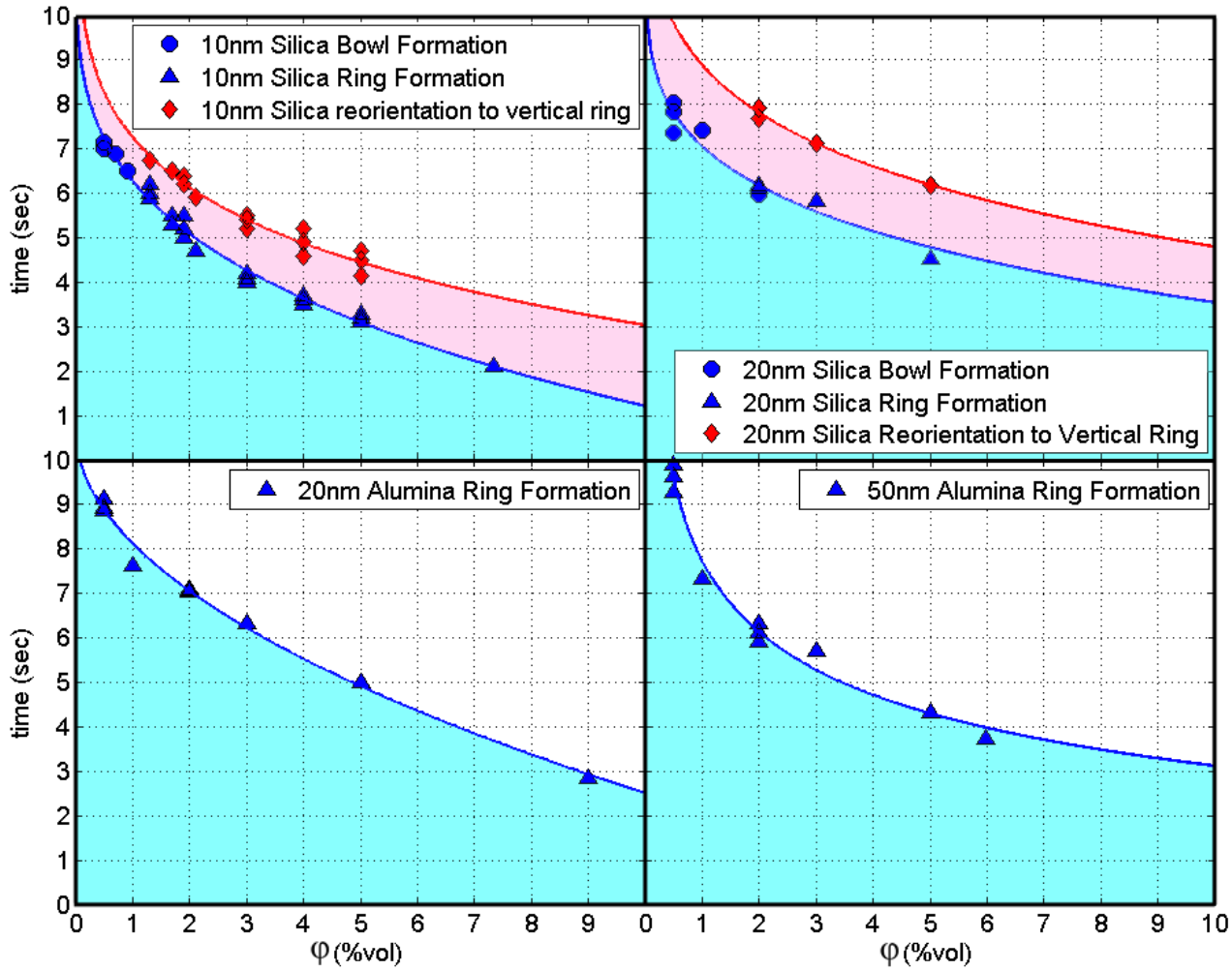

Figure 5.12: Phase diagram comparing different nano-particle solutions, a.) 10nm Silica, b.) 20nm Silica, c.) 20nm Alumina, d.) 50nm Alumina.

Structure reorientation was not seen in the 20nm and 50nm Alumina cases due to the lower recirculation caused by these solutions high viscosity. Relatively slower recirculation and longer structure formation times allow the particles to agglomerate in a more uniform manner forming well defined symmetric structures; this can be seen in the SEM images of the different particle cases presented in figure 5.13.

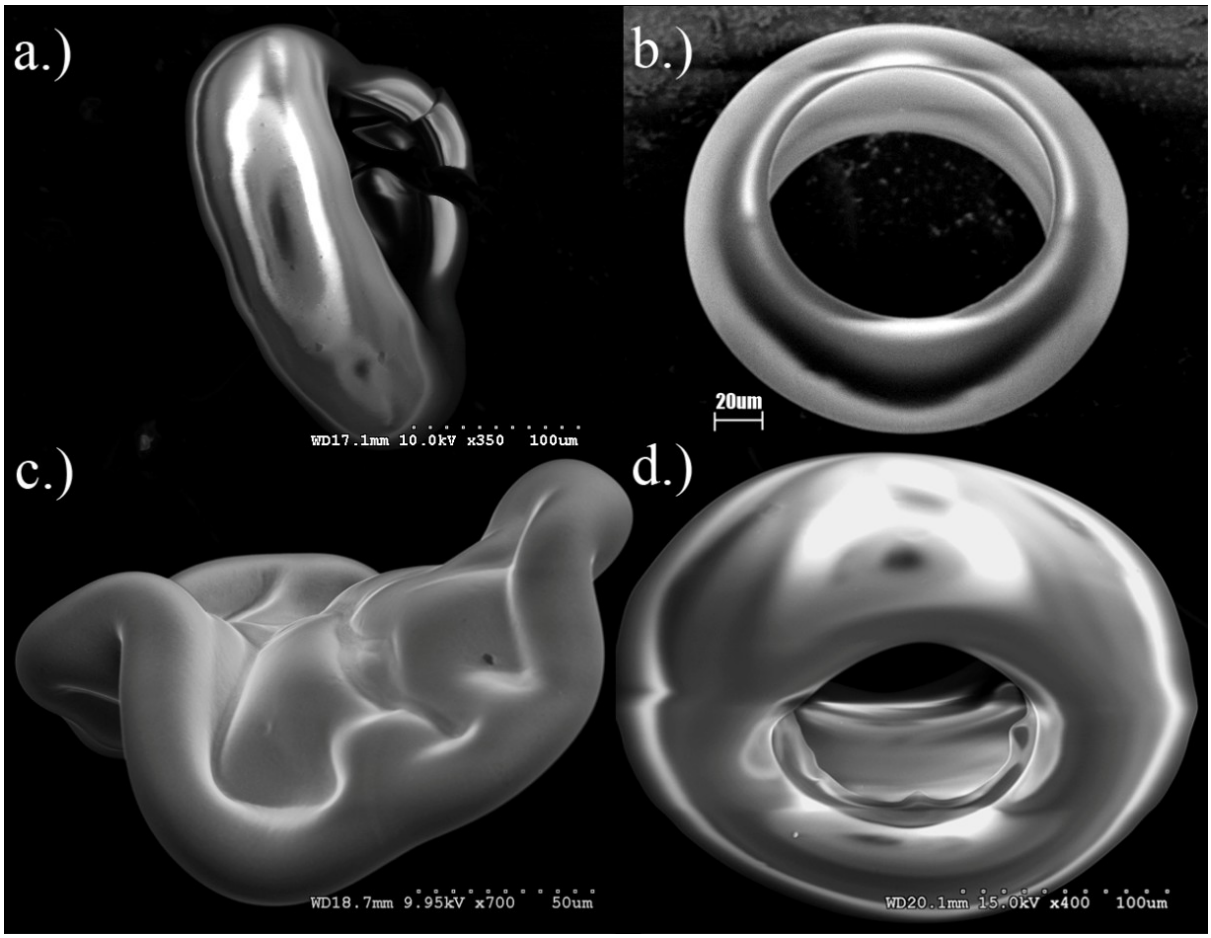

Figure 5.13. Ring SEM images of a.)10nm Silica, b.) 20nm Silica, c.) 20nm Alumina, d.) 50nm Alumina, $\varphi = 2\%$vol.

CHAPTER VI: CONCLUSIONS

In summary, this work shows that there are competing timescales for vaporization, deformation and agglomeration processes. The normalized diameter is inversely proportional to the ratio of agglomeration to evaporation timescales for all concentrations and acoustic amplitudes. It is seen that both agglomeration and evaporation timescales are similar functions of acoustic amplitude (sound pressure level), droplet size, viscosity and density. However it is shown that while the agglomeration timescale decreases with initial particle concentration, the evaporation timescale shows the opposite trend. The final normalized diameter has been shown to be dependent solely on the ratio of agglomeration to evaporation timescales for all concentrations and acoustic amplitudes. The structures also exhibit various aspect ratios (bowls, rings, spheroids) which depend on the ratio of the deformation timescale (t_{def}) and the agglomeration timescale (t_g). A sharp peak in aspect ratio is seen at 10nm Silica ~2% concentration. For $t_{def} < t_g$ a sharp peak in aspect ratio is seen at low concentrations of nanosilica which separates high aspect ratio structures like rings from the low aspect ratio structures like bowls and spheroids.

The correlation between the final structure normalized diameter and the ratio of agglomeration to evaporation time scales holds for different particle types and sizes, this was shown by comparing the results from different particle solutions as function of t_g/t_e. This supports the proposed property based approach to normalizing the structure formation data. Manipulating the precursor solution properties then allows altering the outcome of the structure formation process, such as final structure size and aspect ratio. Increasing solution viscosity has

the resultant effect of decreasing the agglomeration to evaporation time scale ratio, thus yielding larger normalized diameter structures and also affects the final structure morphology such as ring formation at low 10nm Silica concentrations where normally bowls are formed. Similarly, a decrease in surface tension has the overall effect of decreasing t_g/t_e thus increasing final D/D_o, and also decreasing the deformation time scale yielding larger aspect ratio structures favoring the formation of ring structures.

The ratio of agglomeration to evaporation time scales and the ratio of deformation to evaporation time scales determine the final structure morphology. This is seen by the formation of bowls at high t_g/t_e and the formation of rings at low t_g/t_e. Low surface tension favors the formation of rings due to the increase in droplet aspect ratio (Figure 5.6). Solid disc structures, different from hollow ring and bowl structures, form in the case of high viscosity and low surface tension solutions such as 20nm Alumina. The high viscosity of these solutions hinders particle migration, this combined with the resultant high aspect ratio caused by low droplet surface tension yield flat high aspect ratio solid structures.

The duration of the different phases of the structure formation process is determined by the solution properties and the acoustic levitation amplitude (SPL) due to the time scale dependence on these properties. This is seen in the shape of the phase diagrams for different solutions. Finally this work has shown the dependence of the structure formation from functional precursor nanoparticle suspensions on solution viscosity and surface tension and also that the structure formation process can be controlled by manipulating the precursor solution properties and by controlling the acoustic levitation sound pressure level.

LIST OF REFERENCES

[1] W.J. Xie, B. Wei, Appl. Phys. Lett., 90, 204104-1-204104-3, (2007).

[2] W. J. Xie, C. D. Cao, Y. J. Lü, and B. Wei, Phys. Rev. Lett. 89, 104304 (2002).

[3] W. J. Xie and B. Wei, Phys. Rev. E 66, 026605, (2002).

[4] R. Vehring, Pharmaceutical Research,25, No. 5, pp. 999-1022, (2008).

[5] A. Yarin, M. Pfaffenlehner, C. Tropea, J. of Fluid Mechanics, 356, (1998).

[6] Y. Tian Tian, Y., Apfel, R., J. of Aerosol Science, 27, (1996).

[7] A. L. Yarin, G. Brenn, O. Kaster, D. Rensik and C. Tropea, J. of Fluid Mechanics 399, pp. 151-204, (1999).

[8] A.Y. Rednikov, H. Zhao. S.S. Sadhal, E.H. Trinh, J. of the Acoustic Society of Am., 106, pp. 3289-3295, (2006).

[9] E.G. Lierke, Acta Acustica United with Acustica, vol. 88, pp. 206-217, (2002).

[10] D. Milanova and R. Kumar, Appl. Phys. Lett. 95, 133112, (2008).

[11] R. Kumar and D. Milanova, Ann. N.Y. Acad. Sci., 1161, pp. 472-483, (2009).

[12] D. Milanova and R. Kumar, J. Heat Transfer 130, 042401, (2008).

[13] P. Vassallo, R. Kumar, D'Amico, Int. J. Heat and Mass Trans., 47, 407, (2004).

[14] R. Kumar, E. Tijerino, A. Saha, S. Basu, Appl. Phys. Lett. 97, 123106, (2010).

[15] A. Saha, S. Basu, C. Suryanarayana, R. Kumar, Int. J. of Heat and Mass Transfer, Vol. 53, pp. 5663–5674, (2010).

[16] L.G.B. Bremer, P. Walstra, T. van Vliet, Colloids and Surfaces 99, pp. 121-127, (1995).

[17] F. Iskandar, L. Gordon, K. Okuyama, J. Colloid and Interface Science 265, pp. 296-303, (2003).

[18] A. Saha, R.Kumar, S. Basu, Experiments in Fluids, DOI 10.1007/s00348-011-1114-2, (2011).

[19] A. Saha, S. Basu, R. Kumar, J. of Fluid Mechanics, vol. 692, pp 207 – 219, (2012).

[20] V.K. Varadan, A.S. Pillai, D. Mukherji, World Scientific, (2010).

[21] A. Saha, S. Basu, R. Kumar, Physics Letters A, 376, 3185‑3191, (2012).

[22] A.V. Anilkumar, C.P .Lee, T.G. Wang, Physics of Fluids A: Fluid Dynamics, (1993).

[23] Lord Rayleigh. Philosophical Transactions of the Royal Society of London Vol. 175, pp. 1-21, (1884).

[24] A.P. Burdukov, V.E. Nakoryakov, J. of Applied Mechanics and Technical Physics Vol. 6, No. 2, pp. 51-55, (1965).

[25] C.P. Lee and T.G. Wang, J. Acoust. Soc. Am., Vol. 88, Issue 5, pp. 2367-2375, (1990).

[26] N. Riley, Theoretical and Computational Fluid Mechanics, Vol. 10, No. 1-4, pp. 349-356, (1998).

[27] M. Alghane, B.X. Chen, Y.Q. Fu1, Y. Li, J.K. Luo and A.J. Walton, J. of Micromechanics and Microengineering, 21, (2011).

[28] B.G. Loh, S. Hyun, P.I. Ro, J. of the Acoustic Society of Am., 111(2), (2002).

[29] J. M. Howe, Wiley, (1997).

[30] H. Zhao, S.S. Sadhal, J. of the Acoustical Society of Am., Vol. 106, No. 6, pp. 3289-3295, (1999).

[31] Israelachvili, Elsevier, (1991).

[32] H.B. Callen, Wiley, (1985).

[33] G. T. Barnes, I. R. Gentle, Oxford University Press, (2005).

[34] D. Wolf, S. Yip, Chapman and Hall, (1992).

[35] M. Borkovec, W. de Paris, Fractals, Vol. 2. No. 4, pp. 521-526, (1994).

[36] R.H. Chen, T.X. Phuoc, D. Martello, Int. J. of Heat and Mass Transfer, 54, pp. 2459–2466, (2011).

[37] C.T. Nguyen, F. Desgranges, N. Galanis, G. Roya, T. Maréd, S. Boucher, H. Angue Mintsa, Int. J. of Thermal Sciences, 47, pp. 103–111, (2008).

[38] E. Tijerino, R. Kumar, S. Basu, J. Applied Physics, in print (2012).

[39] D.F. Stedman, Trans. Faraday Soc., 24, pp. 289-298, (1928).